

# Chapter 1

## Theoretical Background and Literature

This ability to confine light below the diffraction limit can be achieved by exploiting plasmons. By transferring energy from a diffraction-limited photonic field into resonantly polarised, collective oscillations of conduction electrons an enhanced electric field can be generated on the surface of a metallic nanostructure with nanoscale localisation. It is through the understanding and application of this phenomena that sub-wavelength optics is made possible. This chapter deals firstly with electromagnetic waves in media and the optical properties of metals. From this basis the existence of plasmons can be explained, including the different types of plasmons and how they interact. Finally, the plasmonics of metallic tips is discussed as these are of the structures primary dealt with in this project.

### 1.1 Plasmons

Plasmons are a direct solution of Maxwell's equations at the boundary between a dielectric and a metal. Despite plasmons existing on scale from  $\mathcal{O}(100\text{ nm})$  to  $\mathcal{O}(1\text{ nm})$  the high free electron density of metals means that energy levels still retain their characteristic continuous conduction bands and [quantum/quantisation](#) effects can be ignored. Classical theory is able to accurately describe physical phenomena until the characteristic length scale drops below  $\mathcal{O}(1\text{ nm})$ . A phenomenological approach using Maxwell's equations [1] therefore forms the basis of the mathematical description of plasmons.

#### 1.1.1 Electromagnetic Waves

Maxwell's equations universally describe the classical, dynamical behaviour of electromagnetic (EM) waves and form the foundations of electromagnetism. In their differential form they are

given by,

$$\nabla \cdot \mathbf{E} = \frac{\rho_{\text{tot}}}{\varepsilon \varepsilon_0}, \quad (1.1a)$$

$$\nabla \cdot \mathbf{B} = 0, \quad (1.1b)$$

$$\nabla \times \mathbf{E} = -\frac{\partial \mathbf{B}}{\partial t}, \quad (1.1c)$$

$$\nabla \times \mathbf{B} = \mu \mu_0 \left( \mathbf{J} + \varepsilon \varepsilon_0 \frac{\partial \mathbf{E}}{\partial t} \right), \quad (1.1d)$$

where  $\mathbf{E}$  is the electric field,  $\mathbf{B}$  is the magnetic flux density,  $\varepsilon_0$  is the permittivity of free space,  $\mu_0$  is the permeability of free space,  $\rho_{\text{tot}}$  is the (volume) charge density,  $\mathbf{J}$  is the current density and  $t$  is time. The variables  $\varepsilon$  and  $\mu$  are the relative permittivity and permeability, respectively, and relate to the electromagnetic properties of the medium in which the wave exists. This set of partial differential equations describe the microscopic fields within an electromagnetic system. Two new quantities can be introduced to include material dependencies and describe the macroscopic fields. These are the *electric displacement field*  $\mathbf{D}$  and the *magnetic field*  $\mathbf{H}$ , defined as,

$$\mathbf{D} = \varepsilon_0 \mathbf{E} + \mathbf{P}, \quad (1.2a)$$

$$\mathbf{H} = \frac{1}{\mu_0} \mathbf{B} + \mathbf{M}, \quad (1.2b)$$

where  $\mathbf{P}$  is the polarisation (dipole moment per unit volume) and  $\mathbf{M}$  the magnetisation. The displacement field arises due to polarisation of a material in response to an applied field and is related to the internal charge density by  $\nabla \cdot \mathbf{P} = \rho_{\text{int}}$ . Conservation of charge means that  $\nabla \cdot \mathbf{J} = \partial \rho / \partial t$ , which requires that  $\mathbf{J} = \partial \mathbf{P} / \partial t$  (a result also achievable by differentiating (1.2a)). The final equation of importance is the relationship between the electric field and the current density, given by,

$$\mathbf{J} = \sigma \mathbf{E}, \quad (1.3)$$

where  $\sigma$  is the conductivity. These few relations are sufficient to understand the behaviour of electromagnetic waves in media.

By utilising (1.2a), equations (1.1a) and (1.1d) can be redefined to include material dependencies as,

$$\nabla \cdot \mathbf{D} = \rho_{\text{ext}}, \quad (1.4a)$$

$$\nabla \times \mathbf{H} = \mathbf{J}_{\text{ext}} + \frac{\partial \mathbf{D}}{\partial t}. \quad (1.4b)$$

The charge and current densities now refer to only the external contributions, related to the

internal contributions via  $\rho_{\text{tot}} = \rho_{\text{ext}} + \rho_{\text{int}}$  and  $\mathbf{J}_{\text{tot}} = \mathbf{J}_{\text{ext}} + \mathbf{J}_{\text{int}}$ . Propagation of EM waves within a medium is governed by a wave equation - a partial differential equation relating spatial changes in either the electric or magnetic fields to changes in time. A wave equation describing spatial changes of a wave  $\psi(x)$  along an axis  $x$  in time  $t$  is of the form,

$$\frac{\partial^2 \psi}{\partial x^2} = \frac{1}{v^2} \frac{\partial^2 \psi}{\partial t^2}, \quad (1.5)$$

where  $v$  is the speed of the wave. Combining (1.1c) and (1.1d) leads to the general wave equation for EM waves in the time domain,<sup>1</sup>

$$\nabla(\nabla \cdot \mathbf{E}) - \nabla^2 \mathbf{E} = -\varepsilon \varepsilon_0 \mu \mu_0 \frac{\partial^2 \mathbf{E}}{\partial t^2} - \mu \mu_0 \mathbf{J}, \quad (1.6)$$

$$\nabla(\nabla \cdot \mathbf{D}) - \nabla^2 \mathbf{D} = \frac{\partial^2 \mathbf{D}}{\partial t^2} - \mathbf{J}_{\text{ext}}, \quad (1.7)$$

describing the propagation of an electromagnetic wave in a given medium.

In the absence of both charge and current (1.7) reduces to,

$$\nabla^2 \mathbf{E} = \varepsilon \varepsilon_0 \mu \mu_0 \frac{\partial^2 \mathbf{E}}{\partial t^2}, \quad (1.8)$$

describing a wave propagating in both space and time with a velocity  $c$ . Comparison to (1.5) shows that the speed of light in free space ( $\varepsilon = \mu = 1$ ) is  $c = 1/\sqrt{\varepsilon_0 \mu_0}$ . Furthermore, the refractive index is defined as  $\tilde{n} = \sqrt{\varepsilon \mu}$  such that  $\varepsilon \varepsilon_0 \mu \mu_0 = (\tilde{n}/c)^2 = 1/v^2$ , demonstrating that waves are slowed down by a factor  $\tilde{n}$  inside a medium. In general  $\varepsilon$  is a complex quantity,  $\varepsilon = \varepsilon_1 + i\varepsilon_2$ , and depends on the frequency of the EM wave  $\omega$ . Plasmons are a phenomena resulting from this frequency dependence in metallic materials. The relative permittivity is therefore denoted  $\varepsilon(\omega)$  and is referred to as the dielectric function of a material from this point onwards. For this reason equations are simplified by removing any magnetic contributions by assuming  $\mu = 1$ . Since  $\varepsilon(\omega)$  is a complex parameter  $\tilde{n} = \sqrt{\varepsilon(\omega)} = \sqrt{\varepsilon_1 + i\varepsilon_2}$ , the complex refractive index can be expressed as  $\tilde{n} = n + i\kappa$ , where  $\kappa$  is the extinction coefficient determining absorption in the medium. The complex refractive index and the dielectric function are then related via  $\varepsilon_1 = n^2 - \kappa^2$  and  $\varepsilon_2 = 2n\kappa$ .

If the material dielectric properties in  $\varepsilon$  are linear then  $\mathbf{D}$  can be expressed in Fourier space as,

$$\mathbf{D}(\mathbf{q}, \omega) = \varepsilon_0 \varepsilon(\mathbf{q}, \omega) \mathbf{E}(\mathbf{q}, \omega). \quad (1.9)$$

Combining (1.9) with the differential of (1.2a), (1.3) and a harmonic wave solution<sup>2</sup> yields the

---

<sup>1</sup>Derived using  $\nabla \times \nabla \times \mathbf{E} = \nabla(\nabla \cdot \mathbf{E}) - \nabla^2 \mathbf{E}$

<sup>2</sup> $\partial/\partial t \rightarrow -i\omega$  and  $\mathbf{J} = \dot{\mathbf{D}} - \varepsilon_0 \dot{\mathbf{E}} = \varepsilon_0 \dot{\mathbf{E}}(\varepsilon - 1) = \sigma \mathbf{E}$

relationship between a materials conductivity and its dielectric function,

$$\varepsilon(\mathbf{q}, \omega) = 1 + \frac{i\sigma(\mathbf{q}, \omega)}{\varepsilon_0 \omega}. \quad (1.10)$$

Depending on which is more convenient, either the dielectric function or the conductivity can be used to describe the optical response of a material. Conductivity is typically used to describe lower frequency phenomena while the dielectric function is used at higher frequencies.

The dispersive properties of a material are found by solving (1.7) with  $\varepsilon(\omega)$ , describing the behaviour of a wave propagating through a non-magnetic, dielectric medium. For a monochromatic harmonic wave with frequency  $\omega$  and wave vector  $\mathbf{q}$  in space  $r$  of the form,

$$\mathbf{E} = \mathbf{E}_0 e^{i(\mathbf{q} \cdot \mathbf{r} - \omega t)}, \quad (1.11)$$

representing a propagating EM wave, (1.7) can be expressed in the frequency (Fourier) domain as,<sup>3</sup>

$$\mathbf{q}(\mathbf{q} \cdot \mathbf{E}) - q^2 \mathbf{E} = -\varepsilon(\mathbf{q}, \omega) \frac{\omega^2}{c^2} \mathbf{E}, \quad (1.12)$$

where  $q = |\mathbf{q}|$  is the magnitude of the wavevector. The variable  $q_0^2 = \omega^2/c^2$  is sometimes used in (1.12) when all quantities considered are wave vectors. From this equation the propagation behaviour of EM waves in media can be described.

Solutions to (1.12) depend on the orientation of the wavevector with the field. Transverse wave solutions ( $\mathbf{q} \cdot \mathbf{E} = 0$ ) yield the dispersion relation for light,

$$q = \sqrt{\varepsilon(\mathbf{q}, \omega)} \frac{\omega}{c} = \tilde{n} \frac{\omega}{c}. \quad (1.13)$$

Inserting this into (1.11) gives a general solution for light propagating through a dielectric medium,

$$\mathbf{E}(\mathbf{r}) = \mathbf{E}_0(\mathbf{r}) e^{-\kappa \frac{\omega}{c} \hat{\mathbf{q}} \cdot \mathbf{r}} e^{i\omega(\frac{n}{c} \hat{\mathbf{q}} \cdot \mathbf{r} - t)}. \quad (1.14)$$

The real component of the refractive index  $n$  slows the wave whereas the imaginary component corresponds to an exponential decay with characteristic length  $1/\kappa$ , representing loss within a medium. Since the real part of the conductivity is related to the imaginary part of the dielectric function the decay is attributed to energy transfer into electrons at the surface of the material. Longitudinal wave solutions ( $\mathbf{q} \cdot \mathbf{E} = q|\mathbf{E}|$ ) result in  $\sqrt{\varepsilon(\mathbf{q}, \omega)}\omega/c = 0$  therefore a solution only exists for  $\varepsilon(\mathbf{q}, \omega) = 0$ . Both these conditions are important when describing plasmons. Furthermore, when considering the behaviour of EM waves at an interface between two different media the orientation of the fields with respect to the interface becomes im-

---

<sup>3</sup>Derived using the identities  $\nabla \times \nabla \times \mathbf{E} = \nabla(\nabla \cdot \mathbf{E}) - \nabla^2 \mathbf{E}$ ,  $\nabla^2 \mathbf{E} = -q^2 \mathbf{E}$  and  $\partial^2 \mathbf{E}/\partial t^2 = -\omega^2 \mathbf{E}$  where  $\nabla \cdot \mathbf{E} = 0$

portant. Separate solutions exist depending on if a wave is considered transverse magnetic (TM) or transverse electric (TE) (either only  $\mathbf{E}$  or  $\mathbf{H}$  has a component in the direction of propagating, respectively).<sup>4</sup>

Using the framework outlined so far the optical properties of metals can be deduced along with the existence of plasmons. The discussion begins with the Drude model for the optical response of metals [2], which is used to first predict the behaviour of plasmons. From there the distinction can be made between plasmons within the volume of a metal and those confined to the surface, which are of most interest in plasmonics.

### 1.1.2 Bulk Plasmons and the Optical Properties of Metals

Before studying the concept of a surface plasmon it is important to understand the optical properties of metals in general. When light is incident on a metal, free electrons at the surface respond to the field and are displaced in the opposite direction (since  $\mathbf{F} = -e\mathbf{E}$ ). The field of the induced charge distribution cancels the electric field inside the metal. An electromagnetic wave impinging on a metal is internally screened, and therefore externally reflected<sup>5</sup>, through the displacement of free electrons inside the metal surface. The reflected wave gives metals their shiny appearance. The exponential decay of the wave into the metal, shown in (1.14), is characterised by the skin depth and metals are categorised within the *perfect conductor* approximation. From (1.10) it's known that a high conductivity increases absorption and therefore reduces the field penetration inside the metal. The skin depth is defined as the  $1/e$  point, i.e. the length at which  $q_0 = \kappa$ , giving  $\delta = c/\kappa\omega$ . Light transmission through a metal becomes heavily attenuated once the thickness becomes greater than this value.

A metal becomes more dielectric once the light oscillates fast enough that the inertia of the **massive** electrons means they cannot respond fast enough, preventing screening and thus transmitting the incident light. Such effects begin to be seen around the visible spectrum of light in noble metals. Fields increasingly penetrate the metal until photon energies in the UV spectrum are reached, at which point most metals become transparent. This is known as the *ultraviolet transparency*. These effects can be seen by simply considering the response of a free electron gas to an applied field.

Unlike many other materials whose optical properties are determined by the response of bound electrons (described by the Lorentz oscillator model), the properties of metals are dominated by the response of free electrons delocalised from the positive nuclei background. The Drude model [2] is a simple description of the optical properties of metals and describes the motion of a free electron gas in response to an applied field. The equation of motion for

---

<sup>4</sup>TE and TM are also known as *s*- and *p*-polarisations, respectively.

<sup>5</sup>Light absorbed by electrons will be re-emitted, or from a different point of view, the prevention of light from entering the metal means the incident field must be reflected.

a single electron in a time-varying applied field is given by,

$$m\ddot{\mathbf{x}}(t) + m\gamma\dot{\mathbf{x}}(t) = -e\mathbf{E}(t), \quad (1.15)$$

where  $m$  is its effective optical mass and  $\gamma = 1/\tau$  is the electron collision frequency, the inverse of the relaxation time  $\tau$ . Use of an effective optical mass as opposed to the actual electron mass incorporates band structure effects into the model. The electron collision frequency amounts to an effective coefficient of damping as in a mechanical oscillator. Inserting a harmonic driving field and assuming a similar oscillatory behaviour in the free electron displacement ( $\mathbf{x} = \mathbf{x}_0 e^{-i\omega t}$ ) leads to a solution,

$$\mathbf{x}(t) = \frac{e}{m(\omega^2 + i\gamma\omega)} \mathbf{E}(t). \quad (1.16)$$

There is a resulting polarisation  $\mathbf{P} = -nex$ , where  $n$  is the number density of electrons, induced in the free electron gas. The resulting displacement field, acquired by substituting (1.16) into (1.9)<sup>6</sup>, defines the dielectric function of a metal,

$$\varepsilon(\omega) = 1 - \frac{\omega_p^2}{\omega^2 + i\gamma\omega}, \quad (1.17)$$

where  $\omega_p$  is the plasma frequency of the metal, given by,

$$\omega_p^2 = \frac{ne^2}{\varepsilon_0 m}. \quad (1.18)$$

The optical properties of a metal can be discerned from the real and imaginary components of  $\varepsilon(\omega)$ , given by,

$$\text{Re}[\varepsilon(\omega)] = \varepsilon_1(\omega) = 1 - \frac{\omega_p^2 \tau^2}{1 + \omega^2 \tau^2}, \quad (1.19a)$$

$$\text{Im}[\varepsilon(\omega)] = \varepsilon_2(\omega) = \frac{\omega_p^2 \tau}{\omega(1 + \omega^2 \tau^2)}. \quad (1.19b)$$

Metallic physical characteristics correspond to  $\text{Re}[\varepsilon(\omega)] < 0$ , i.e. D negative compared to E, where electrons move to oppose an incident field. The plasma frequency defines the point at which the metal transitions into a dielectric. For  $\omega < \omega_p$ ,  $\text{Re}[\varepsilon(\omega < \omega_p)] < 0$  and a free electron gas remains metallic in character. Once  $\omega > \omega_p$  the free electron gas, limited by inertia, cannot respond fast enough to follow the field and becomes dielectric in character.

---

<sup>6</sup>Derived from  $\mathbf{D} = \varepsilon_0 \mathbf{E} + \mathbf{P} = \varepsilon_0 \mathbf{E} - [ne^2/m(\omega^2 + i\gamma\omega)] \mathbf{E} = \varepsilon_0 \varepsilon(\omega) \mathbf{E}$

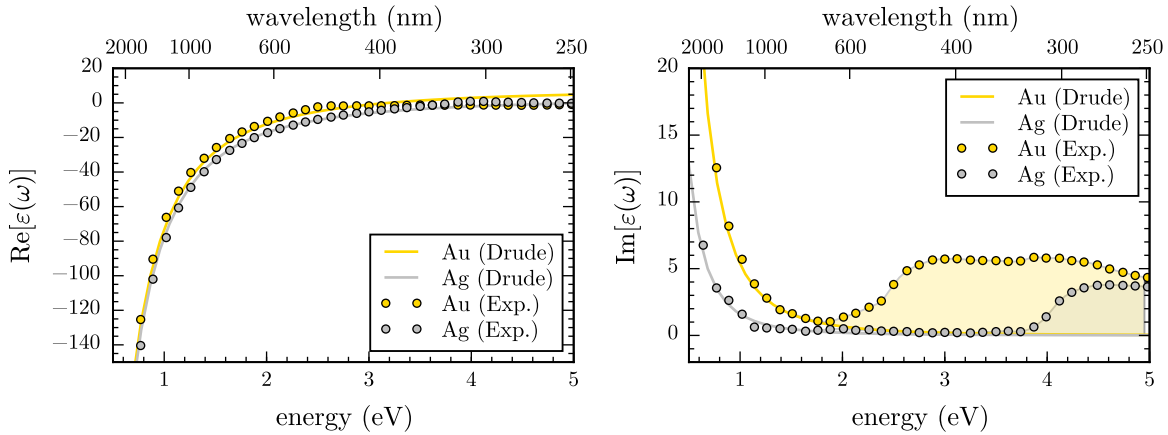


**Figure 1.1:** Plot of the dielectric function, given by the Drude model, for Au and Ag compared with empirical data.  $\varepsilon(\omega)$  is calculated using (1.21). The plasma frequency is calculated using (1.18). The parameters of the curves are  $n = 5.90 \times 10^{28} \text{ m}^{-3}$ ,  $m = 9.11 \times 10^{-31} \text{ kg}$ ,  $\gamma = 1/\tau = 1/1 \times 10^{-14} \text{ s}$  and  $\varepsilon_\infty = 8$  for Au and  $n = 5.86 \times 10^{28} \text{ m}^{-3}$ ,  $m = 9.11 \times 10^{-31} \text{ kg}$ ,  $\gamma = 1/\tau = 1/3 \times 10^{-15} \text{ s}$  and  $\varepsilon_\infty = 3$  for Ag. Empirical data (Johnson and Christy, 1972 [3]) is shown for comparison to illustrate the importance of interband transitions. Deviations from the Drude model due to interband transitions are shaded.

For an ideal free electron gas with negligible damping the expression,

$$\varepsilon(\omega) = 1 - \omega_p^2/\omega^2, \quad (1.20)$$

is often used. This is the often the case for large (optical) frequencies close to  $\omega_p$  where the imaginary component of  $\varepsilon(\omega)$ , dominated by  $\omega\tau \gg 1$ , becomes negligible. In actually, however, interband transitions in real metals increase  $\text{Im}[\varepsilon(\omega)]$ . The expression for the dielectric function can be modified to account for interband absorption caused by bound electrons by the inclusion of a constant  $\varepsilon_\infty$ . The dielectric function then has the form,

$$\varepsilon(\omega) = \varepsilon_\infty - \frac{\omega_p^2}{\omega^2 + i\gamma\omega}. \quad (1.21)$$

Plotting (1.21), along with empirical data, illustrates both why noble metals exhibit high quality visible spectrum (400–700 nm, 1.5–3 eV) plasmonics as well as the failings of the Drude model. Noble metals have  $\text{Re}[\varepsilon(\omega)] < 0$  and small  $\text{Im}[\varepsilon(\omega)]$  in the visible region, hence behave very similar to an ideal free electron gas. The Drude model fails at higher energies as interband transitions are not included in the basic model. These transitions increase the absorption ( $\propto \text{Im}[\varepsilon(\omega)]$ ) and are significant for  $\lambda < 500 \text{ nm}$  in Au and  $\lambda < 300 \text{ nm}$  in Ag. A measure of the quality of a plasmonic material can de determined from its quality factor  $Q = |\text{Re}[\varepsilon]/\text{Im}[\varepsilon]|$ . The high  $Q$  of noble metals in the visible regions means they can easily respond to an incident field and screen it, behaving well plasmonically. Interband transitions

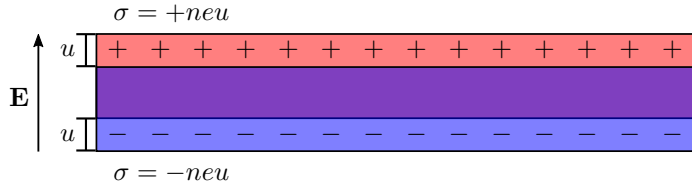


**Figure 1.2: Charge displacement of a free electron gas under an applied field.** The optical electric field displaces the electrons leaving behind the positive cores. The slab becomes polarised with opposing surface charge densities  $\sigma$ . The charge oscillations resonate when the field frequency is  $\omega_p$ .

lead to a reduction in  $Q$  at higher energies therefore preventing good plasmonics.

The significance of the plasma frequency  $\omega_p$  in  $\epsilon(\omega)$  is that it not only describes a metal-to-dielectric transition but also dictates the frequency of the collective longitudinal mode of oscillation. By substituting (1.20) into the dispersion relations for transverse and longitudinal waves it is clear that transverse waves are only supported if  $\omega > \omega_p$  (dispersion:  $\omega^2 = \omega_p^2 + q^2 c^2$ ). However, a collective longitudinal oscillation is allowed at  $\omega = \omega_p$  since  $\epsilon(\omega) = 0$  in the absence of damping. In this case the free electron gas is displaced from the ionic core background a distance  $u$  due to the applied field to form surface charge densities  $\sigma = \pm neu$ . The resulting depolarisation field<sup>7</sup> is  $\mathbf{E} = neu/\epsilon_0$  and the motion of the free electrons are defined by,

$$nm\ddot{u} = -ne\mathbf{E} = -\frac{n^2 e^2 u}{\epsilon_0}. \quad (1.22)$$

Simplifying this relation leads to,

$$\ddot{u} + \omega_p^2 u = 0, \quad (1.23)$$

hence  $\omega_p$  is considered the natural frequency of the system and the electrons resonate when driving at  $\omega = \omega_p$ . This is known as the bulk or *volume plasmon*. Since this is a longitudinal oscillation, however, light cannot couple with a volume plasmon. Experimentally these are measured using electron energy loss spectroscopy (EELS), whereby colliding electrons impart energy and excite a volume plasmon []. Observation of optical plasmonic phenomena therefore means that light-matter plasmonics is the result of a different kind of plasmon.

### 1.1.3 Surface Plasmons, Surface Plasmon Polaritons and Localised Surface Plasmon Polaritons

Surface plasmons (SPs), unlike bulk plasmons, are tightly confined to the surface of the metal. Unlike in the bulk of a metal, electrons displaced by an applied field at the surface of a metal do feel a restoring force with the positive nuclei background. Transverse fields impinging on the

---

<sup>7</sup>Gauss' law  $\int \mathbf{E} \cdot d\mathbf{A} = Q/\epsilon_0 = \sigma A/\epsilon_0$ , hence  $\mathbf{E} = \sigma/\epsilon_0$ . Alternatively  $D = 0 = \epsilon_0 \mathbf{E} + \mathbf{P}$  therefore  $\mathbf{E} = -\mathbf{P}/\epsilon_0 = -ne\mathbf{u}/\epsilon_0$ .

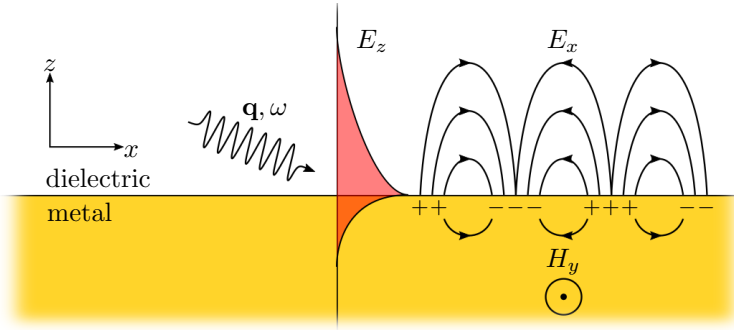


**Figure 1.3: Diagram of a surface plasmon polariton (SPP).** TM surface electron density waves couple with an evanescent wave from a TM EM wave to form a SPP.

metal surface at an angle are then able to manipulate the electron motion. SPs can therefore be manipulated by light as well as by the longitudinal waves needed to excite bulk plasmons. These form polariton quasiparticles under strong coupling with photons and are therefore optically excitable under the right conditions.<sup>8</sup> The most commonly considered plasmon is the surface plasmon polariton (SPP), a propagating TM wave confined to the surface of a metal. It is the bound state between a photon and a surface plasmon, resulting from EM wave excitation of SPs. While confined in two dimensions to the planar boundary between a metal-dielectric interface the plasmon can either propagate or become stationary as a result of interference with itself or other plasmons. The latter stationary form of the SPP is similar to the localised surface plasmons described later.

The SPP itself is described through its dispersion, or more specifically, by its wavevector,  $\mathbf{q}$ , and its angular frequency,  $\omega$ . As a TM wave propagating along a metal/dielectric interface the field profile is given by  $\mathbf{E}(\mathbf{x}) = \mathbf{E}(z)e^{i\beta x}$  where  $\beta = q_x$  is the propagation constant. The magnetic field in this configuration is therefore given by  $\mathbf{H}(\mathbf{x}) = \mathbf{H}(y)e^{i\beta x}$ . The behaviour of such a wave in (1.12) is,

$$\frac{\partial^2 \mathbf{E}(z)}{\partial z^2} + (q_0^2 \epsilon - \beta^2) \mathbf{E} = 0, \quad (1.24a)$$

$$\frac{\partial^2 \mathbf{H}(y)}{\partial y^2} + (q_0^2 \epsilon - \beta^2) \mathbf{H} = 0, \quad (1.24b)$$

which can be solved under the appropriate boundary conditions to yield the properties of a SPP. Assuming a TM wave ( $\partial E_y / \partial z = 0$ ,  $\partial H_z / \partial z = 0$ ), propagation only in the  $x$  direction

---

<sup>8</sup>Polaritons are the name given to quanta or quasiparticles of light-matter interactions. Strong coupling describes the point at which a quasiparticle is no longer distinguishable between its two constituent components.

and symmetry in  $y$  results in the following outcomes from (1.1c) and (1.1d),

$$E_x = -i \frac{1}{\omega \varepsilon_0 \varepsilon} \frac{\partial H_y}{\partial z}, \quad (1.25a)$$

$$E_z = -\frac{\beta}{\omega \varepsilon_0 \varepsilon} H_y. \quad (1.25b)$$

In this instance the TM wave equation, and requirement for evanescent decay in the  $z$  direction, mean that  $H_y = A_2 e^{i\beta x} e^{q_2 z}$  for  $z > 0$  (in the dielectric) and  $H_y = A_1 e^{i(\beta x)} e^{q_1 z}$  for  $z < 0$  (in the metal). The components of the electric field can therefore be expressed as,

$$E_x(z) = i A_2 \frac{1}{\omega \varepsilon_0 \varepsilon_2} q_2 e^{i\beta x} e^{-q_2 z}, \quad (1.26a)$$

$$E_z(z) = -A_1 \frac{\beta}{\omega \varepsilon_0 \varepsilon_2} e^{i\beta x} e^{-q_2 z}, \quad (1.26b)$$

inside the dielectric and,

$$E_x(z) = -i A_1 \frac{1}{\omega \varepsilon_0 \varepsilon_1} k_1 e^{i\beta x} e^{k_1 z}, \quad (1.27a)$$

$$E_z(z) = -A_1 \frac{\beta}{\omega \varepsilon_0 \varepsilon_1} e^{i\beta x} e^{k_1 z}, \quad (1.27b)$$

inside the metal, where  $\varepsilon_1 = \varepsilon_m$  and  $\varepsilon_2 = \varepsilon(\omega)$  in the previously used notation. Continuity across the boundary ( $z = 0$ ) dictates that  $A_1 = A_2$  and yields the relation,

$$\frac{k_2}{k_1} = -\frac{\varepsilon_2}{\varepsilon_1}, \quad (1.28)$$

hence the ratio between wavevectors inside and outside of the metal depends on the relative change in dielectric constant across the boundary. It is this continuity relation that allows for the existence of SPPs in the TM configuration, unlike for TE waves for which this result is not possible and there can be no SPPs. To determine the SPP propagation constant  $\beta$  a further relation is needed to fix the wave vectors in a given medium with respect to the dielectric constant. Using the expression for  $H_y$  in the wave equation (1.12) yields a set of relations,

$$k_1^2 = \beta^2 - k_0^2 \varepsilon_1, \quad (1.29a)$$

$$k_2^2 = \beta^2 - k_0^2 \varepsilon_2, \quad (1.29b)$$

which, when combined with (1.28), fully describe the fields around the interface. The SPP propagation constant is then given by,

$$\beta = \frac{\omega}{c} \sqrt{\frac{\varepsilon_1 \varepsilon_2}{\varepsilon_1 + \varepsilon_2}}. \quad (1.30)$$

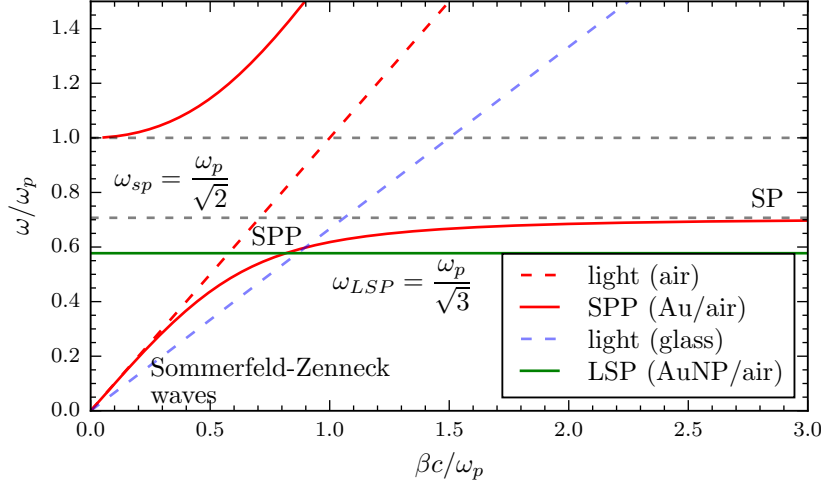


**Figure 1.4: Plasmon dispersion relations for the SPP and LSP.** The dashed lines indicate the dispersion of light in both glass and air (vacuum) along with the surface plasmon frequency. SPPs can be described as photon-like or plasmon-like depending on their point of excitation. SPPs excited with large  $q$  and  $\omega \approx \omega_{SPP}$  are considered plasmon-like while SPPs with low  $q$  are considered more photon-like.

This is the dispersion relation for a SPP and describes many of the important properties of a plasmon.

The SPP dispersion described by (1.30) is shown in Figure 1.4 along with the dispersion of light for both air and glass media. From the dispersion curve it is clear that SPPs cannot couple with light within the same medium as their dispersion curves do not cross. However, light from within a high refractive index medium such as glass can excite SPPs on a metal/air interface via evanescent waves. This method of coupling photons with surface plasmons, depending on the specific prism arrangement, is known as the Kretschmann (prism-metal-dielectric) or Otto (prism-dielectric-metal) configuration [4, 5]. Since a diffraction grating may also impart momentum onto a photon ( $q_x \rightarrow q_x + n\pi$ ) a metallic grating launch SPPs along a planar metal-dielectric interface [6]. This phenomenon was first observed in 1902 by Wood, dubbed as Wood's anomaly [6], and only explained via surface waves many years later [7].

Closer inspection of the curve highlights one of the major features of a plasmon. While SPPs retain the frequency of the excitation field, their wavelength is considerably smaller than the diffraction limited wavelength of light. Depending on where on the curve the SPP lies it can be considered to be either more photon-like or more plasmon-like. For small  $\beta \approx q_0$  the SPP is similar to light grazing the interface whereas SPPs with large  $k$  become more plasmon-like and the frequency saturates at the surface plasmon frequency,

$$\omega_{sp} = \frac{\omega_p}{\sqrt{1 + \varepsilon_d}}. \quad (1.31)$$

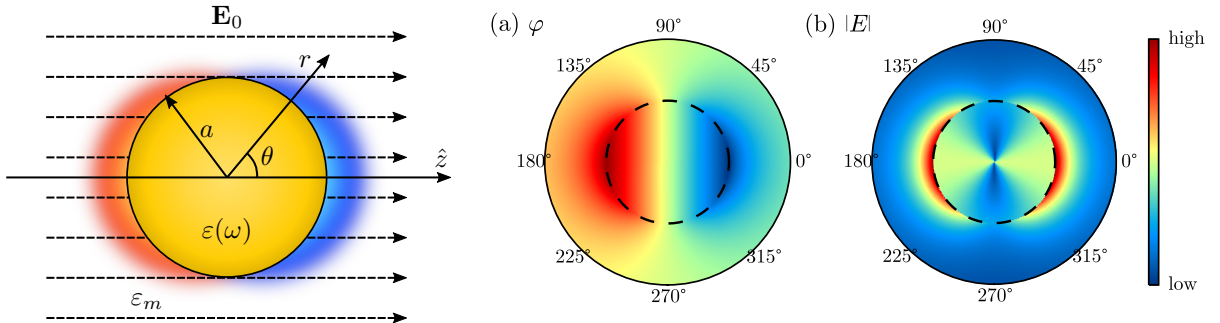


**Figure 1.5: A spherical metallic particle in an applied electric field.** The sphere is assumed to be in the quasistatic regime ( $a \ll \lambda$ ). The aura around the particle indicates the phase of the free electron oscillations in the plasmon. Calculations of (a) the potential and (b) the magnitude of the electric field for a spherical nanoparticle on resonance ( $\epsilon(\omega) = -2\epsilon_d$ ).

At this point the SPP can be considered electrostatic and becomes a *surface plasmon* (SP). SPs are standing waves and can be formed by interference between counter-propagating SPPs. To some extent, SPs confined to a finite, continuous, non-planar surface, defining a nanoparticle (NP), can be considered to be the basis for a localised surface plasmon (LSP) or localised surface plasmon polariton (LSPP).

LSPs are collective oscillations of conduction electrons confined within a fixed sub-wavelength spatial extent, usually on the surface of a metallic nanoparticle (MNP). Free electrons are displaced from the nuclei in response to an applied field and form a surface charge distribution, polarising the particle. Coulomb interaction between the poles of the surface charge distribution results in a restoring force within the particle. This gives rise to a natural frequency of oscillation, leading to a surface plasmon resonance (SPR) when driven harmonically at the correct frequency. The particle geometry sets which multipolar surface charge distributions are supported while its material properties and the dielectric properties of the surrounding medium set the restoring force. Each different multipolar charge distribution is therefore considered to be a unique LSP mode, identifiable by its SPR. This bears some similarity with the slab of free electron gas supporting volume plasmons, shown in Figure 1.2, except that the sub-wavelength geometry modifies the restoring force. The plasma frequency in LSPs is then rescaled by a factor depending on the geometry of each LSP mode.

The simplest form of a LSP is the dipole resonance of a spherical MNP. Assuming the sphere radius,  $a \ll \lambda$ , the wavelength of light, the particle is considered to be in the quasistatic regime and electrostatics, rather than electrodynamics, is applicable to solve the problem. The electrostatic potential,  $\varphi$ , of the system is then described by the Laplace equation,  $\nabla^2\varphi = 0$ , with a general solution in a spherical geometry of the form,

$$\varphi_{l,m_l}(r, \theta, \phi) = \sum_{l=0}^{l=\infty} \sum_{m_l=-l}^l [A_l r^l + B_l r^{-(l+1)}] P_l^m(\cos \theta) e^{im_l \phi}, \quad (1.32)$$

where  $l$  is the degree of spherical harmonic and  $m_l$  its projection,  $A_l$  and  $B_l$  are constants and  $P_l^m(\cos \theta)$  are associated Legendre polynomials. For a sphere of radius  $a$  and dielectric function  $\varepsilon(\omega)$  in a dielectric medium described by  $\varepsilon_d$  the solution is fixed by the boundary condition  $\varphi_{\text{out}} \rightarrow -E_0 z$  as  $r \rightarrow \infty$  and by matching the potential gradient at the metal-dielectric interface at  $r = a$ . This reduces to a solution [8],

$$\varphi = \begin{cases} -\frac{3\varepsilon_d}{\varepsilon(\omega) + 2\varepsilon_d} \mathbf{E}_0 \cdot \mathbf{r} & r \leq a \text{ (inside)}, \\ \left( -1 + \frac{\varepsilon(\omega) - \varepsilon_d}{\varepsilon(\omega) + 2\varepsilon_d} \frac{a^3}{r^3} \right) \mathbf{E}_0 \cdot \mathbf{r} & r > a \text{ (outside)}. \end{cases} \quad (1.33)$$

For a metal sphere the potential describes an induced dipolar surface charge distribution, as plotted in Figure 1.5a. The description is simplified by defining the dipole moment as,

$$\mathbf{p} = \varepsilon_0 \varepsilon_d \alpha \mathbf{E}_0 = 4\pi \varepsilon_0 \varepsilon_d a^3 \frac{\varepsilon(\omega) - \varepsilon_d}{\varepsilon(\omega) + 2\varepsilon_d} \mathbf{E}_0, \quad (1.34)$$

where the polarisability,  $\alpha$ , incorporates the frequency dependent behaviour and is defined as,

$$\alpha(\omega) = 4\pi a^2 \frac{\varepsilon(\omega) - \varepsilon_d}{\varepsilon(\omega) + 2\varepsilon_d}. \quad (1.35)$$

The outside potential is then expressed as,

$$\varphi_{\text{out}} = -\mathbf{E}_0 \cdot \mathbf{r} + \frac{\mathbf{p} \cdot \mathbf{r}}{4\pi \varepsilon_0 \varepsilon_d r^3}. \quad (1.36)$$

The potential of the system is simply the potential of a dipole superimposed onto the incident field. The field inside and outside of the sphere is calculated using  $\mathbf{E} = -\nabla \varphi$  and is given by,

$$\mathbf{E} = \begin{cases} \frac{3\varepsilon_d}{\varepsilon(\omega) + 2\varepsilon_d} \mathbf{E}_0 & r \leq a \text{ (inside)}, \\ \mathbf{E}_0 + \frac{3\mathbf{n}(\mathbf{n} \cdot \mathbf{p}) - \mathbf{p}}{4\pi \varepsilon_0 \varepsilon_d} \frac{1}{r^3} & r > a \text{ (outside)}, \end{cases} \quad (1.37)$$

where  $\mathbf{n} = \mathbf{r}/r$  is the unit vector. As with the potential, the electric field is the superposition of the incident field with the field emitted from a point dipole, shown in Figure 1.5b.

Due to its assumed small size  $a \ll \lambda$  it is assumed that the electrons in the sphere can respond instantaneously to the incident field and phase retardation is ignored (quasistatic approximation). The electrostatic result is then simply multiplied with a harmonic time dependence to describe the electrodynamic behaviour. Therefore, when illuminated by a plane wave  $\mathbf{E}_0 e^{i\omega t}$  the induced dipole moment oscillates like  $\mathbf{p} e^{i\omega t}$ . In this sense the coherent oscillation of free electrons in the sphere is considered to be an oscillating point dipole source given by  $\mathbf{p} e^{i\omega t} = \varepsilon_0 \varepsilon_d \alpha \mathbf{E}_0 e^{i\omega t}$ . The physical behaviour of the electrons in the sphere, described

using the dielectric function  $\varepsilon(\omega)$ , is then simply incorporated into  $\alpha(\omega)$ , at which point its frequency dependence becomes important.

For a good metal  $\text{Re}[\varepsilon(\omega)] < 0$  and therefore the denominator in (1.35) can undergo resonance **wherein/whereby**  $\alpha \rightarrow -\infty$  when  $\varepsilon(\omega) + 2\varepsilon_d \rightarrow 0$ . This dipolar resonance occurs at the Fröhlich condition,

$$\text{Re}[\varepsilon(\omega)] = -2\varepsilon_d. \quad (1.38)$$

It's strength in realistic metals is restricted by damping of the electron motion leading to a Lorentzian-shaped resonance band. Resonant excitation of an induced oscillating dipole moment therefore corresponds to excitation of a collective oscillation of conduction electrons on the surface of the sphere - the fundamental dipolar LSP. On resonance, this enhanced dipole strongly opposes the applied field. As seen in (1.37), the field from the induced dipole moment of the plasmon is superimposed onto the incident field leading to a near-field enhancement both inside and outside the surface of the sphere. This is one of the fundamental properties of the plasmon, and one that is most exploited in sensing and sensor developments.

Under the Drude model, with  $\varepsilon(\omega)$  given by (1.21), the Fröhlich condition is satisfied when,

$$\omega = \frac{\omega_p}{\sqrt{1 + 2\varepsilon_d}}, \quad (1.39)$$

which evaluates to  $\omega = \omega_p/\sqrt{3}$  for a MNP in vacuum. As can be seen in Figure 1.4, the flat dispersion of a LSP mode means it crosses the light line at a single point, hence light of the correct frequency can readily couple with LSPs without the need for SPP momentum matching mechanisms. In general the optical spectrum of a MNP can contain a number of plasmon modes for which the resonant frequencies are given by,

$$\omega_l = \omega_p \sqrt{\frac{l}{\varepsilon_d(l+1)+1}}, \quad (1.40)$$

where the degree of spherical harmonics  $l$  denote the charge distribution and denoted mode order ( $l = 1$  for dipole,  $l = 2$  for quadrupole, etc.). However, these modes only exist outside of the quasistatic regime and are therefore only observed in larger MNPs [] or more complex geometries []. For plasmonically-active nobles metals, such as Au and Ag, the fundamental  $l = 1$  mode occurs in the visible spectrum ( $\lambda = 520$  nm for Au and  $\lambda = 360$  nm for Ag), which is why they are so often used in optics. Additionally, since the polarisability changes with NP geometry, changes from a spherical shape lead to tuning of the resonances across the visible spectrum. This geometrical dependence is well known and has been measured experimentally on a number of occasions [9, 10].

As with any oscillating **dipole/charge distribution**, energy is both absorbed and emitted from the plasmon. The oscillating charge has the ability to scatter the incident planar field

into spherical waves. The excitation of a resonant dipolar oscillation means that the scattering is also resonantly enhanced. The balance between the absorbance and the scattering from a MNP is dictated by its size. The absorbance and scattering cross sections are given by [11],

$$\sigma_{\text{scat}} = \frac{q^4}{6\pi} |\alpha|^2 = \frac{8\pi}{3} q^4 a^6 \left| \frac{\varepsilon(\omega) - \varepsilon_d}{\varepsilon(\omega) + 2\varepsilon_d} \right|^2, \quad (1.41\text{a})$$

$$\sigma_{\text{abs}} = q \text{Im}[\alpha] = 4\pi q a^3 \text{Im} \left[ \frac{\varepsilon(\omega) - \varepsilon_d}{\varepsilon(\omega) + 2\varepsilon_d} \right]. \quad (1.41\text{b})$$

The extinction cross section, commonly used in spectroscopy, can be calculated using  $\sigma_{\text{ext}} = \sigma_{\text{scat}} + \sigma_{\text{abs}}$ . Since they depend on  $\alpha$  the size of the cross section, i.e. the spatial extent over which light can interact with the MNP, is increased on resonance. This is why MNPs appear strongly coloured and much larger in optical microscopy than they actually are. The absorbance and scattering cross sections scale as  $a^3$  and  $a^6$ , respectively, hence larger particles scatter more than they absorb whereas smaller particles absorb more [1]. From these equations the optical antenna properties of a MNP become clearer. The LSP state mediates energy transfer from the nanoscale to the microscope scale, and vice-versa. On resonance with the dipolar LSP, both cross sections are enhanced **up to  $10^6$**  by the polarisability resonance from  $\mathcal{O}(a \sim 50 \text{ nm})$  to  $\mathcal{O}(1 \mu\text{m})$ , therefore efficiently couple with photons in the far-field.<sup>9</sup> The plasmon acts to match the electromagnetic modes of a nanoscale absorber/emitter with those of a diffraction-limited photonic mode via an oscillating charge density, hence a plasmonic particle is described as an *optical antenna* in a similar manner to a device that converts radio waves into an electrical current is named a radio antenna.

Whilst the quasistatic approach is useful to first demonstrate the enhancing capabilities of a MNP, the description breaks down once the size of the particle becomes more comparable to the excitation wavelength. Retardation effects between the field and the electrons mean that phase differences between the charge oscillations and the incident field become important. At this point Mie theory (electrodynamics) is required to describe the spectral response of spherical MNPs [12]. Mie theory provides a more general description of the optical response of spherical MNPs. Using this approach the spectra of a MNP can be decomposed into superimposed multipoles, alluding to the existence of higher order LSP modes in larger MNPs. The spectral response of spherical AuNPs of varying sizes is shown in Figure 1.6, demonstrating the redshift and broadening of lower order modes with increasing particle size and the excitation of higher order modes.

Furthermore, from Figure 1.6, the scattering cross section for more realistically modelled MNPs is enhanced by a not insignificant factor, even when compared with the much higher enhancement from the electrostatic result. This again explains why diffraction-limited light

---

<sup>9</sup>Consider that  $\sigma_{\text{scat}}$  for a AuNP is enhanced  $100\times$  on resonance, meaning it's cross section is  $\sqrt{100/\pi} = 6\times$  wider than it's radius, hence why a 50 nm AuNP looks like a 300 nm green sphere when imaged.

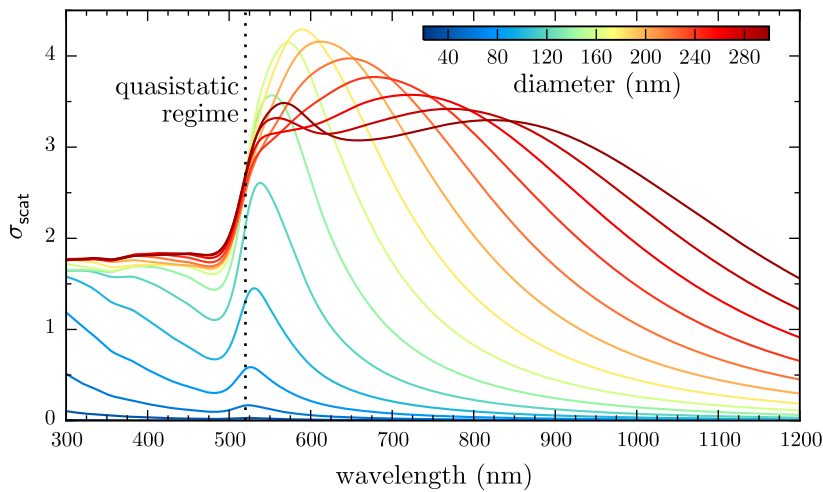


**Figure 1.6: Mie scattering efficiencies/cross-sections for AuNPs of increasing diameter.** The 520 nm resonance position of the dipolar LSP mode of a AuNP in the quasistatic approximation is indicated by the dotted line. The resonance stays at 520 nm until  $d > 80$  nm then redshifts. The emergence of higher order modes following a similar behaviour is seen once  $d > 100$  nm.

efficiently couples well with metallic nanostructures. The increased cross sections acts as a means of mode-matching the similarly sized incident fields with the nanoscale geometry. LSPs can therefore effectively mediate the interactions between photons and nanoscale electromagnetic, such as phonons (Raman) and radiative energy levels (quantum emitters, fluorescence) [13]. Plasmonic modes which readily couple with the far-field in this manner are therefore sometimes referred to as *antenna modes* and become important when designing resonant structures for specific sensing applications.

#### 1.1.4 Geometrical Influences on Antenna Modes

So far only a spherical geometry has been considered. As stated previously, the LSP is a geometrical resonance and exists primarily due to the interplay between the driving field inducing oscillations in the mobile electrons and the resulting restoring force acting between the positive ionic core background and the accumulation of conduction electrons at the surface. While the surface charge oscillation directly correlates to the driving field the restoring force is geometry dependent. The plasmon resonance of a single particle is therefore very geometry dependent [krenn2002, 9, 10]. The larger the separation between opposing surface charge poles in the antenna, the weaker the restoring force. As seen with Mie theory, a larger particle with a smaller restoring force has a lower energy resonance. The same can be said if the particle geometry is elongated. Its polarisability is adjusted to account for this by inserting a geometrical correction, Inevitably continual separation of the poles weakens the restoring force so much that the antenna plasmon resonance no longer exists. For the case where there

is no restoring force electrons respond directly in anti-phase to the incident field until the field oscillates too quickly for the electrons to follow, i.e.  $\omega > \omega_p$ . Under these conditions there is no resonance.

Mathematically the restoring force physics is incorporated into the resonant polarisability transformation from a spherical particle into an ellipsoid

By utilising the particle material, geometry and polarisation anisotropy to tune the plasmon resonance, the resonant wavelength band can be shifted across the entire UV–NIR spectrum to tailor individual applications. The limitation to this technique is the restricted field enhancement that a single particle can provide. An alternative approach to exploiting LSPs is therefore to couple the fields of many plasmons together. Through coupling the confined fields in the gaps between MNPs can be enhanced by many more orders of magnitudes.

## 1.2 Plasmon Coupling

Both the resonant field enhancement and the confinement of a surface plasmon can be improved by bringing a second plasmon into close proximity. Similar to coupled harmonic oscillators and dipoles, plasmons couple together once in close proximity. Normal modes of oscillation are formed once the charge distribution of one plasmon strongly couples via Coulomb forces with the charge distribution of an adjacent plasmon. In many cases the resulting normal mode has its charge distribution strongly confined to the dielectric space between metallic surfaces where charges interact most. Normal modes are therefore more generally known as *gap plasmons*.

Coupling between plasmons is a feature of many metallic systems with closely spaced metal-dielectric interfaces, including metal-insulator-metal (MIM) and insulator-metal-insulator (IMI) waveguides and systems containing multiple MNPs. For the purposes of this work, further discussion is restricted to the ideal case of coupled LSPs between two closely spaced MNPs, though the coupling description is valid for many other cases involving SPs.

### 1.2.1 Localised Surface Plasmon Hybridisation in Plasmonic Nano-Gap Cavities

In the simplest case, only multipolar plasmons, excited in two isolated spherical MNPs being driven by external fields, are considered. This is the prototypical plasmonic dimer system used to understand plasmon coupling. Similar systems, including chains of MNPs [15] and MNP mirror charges [16], have been used to study plasmon coupling. As the plasmons move closer together the force between charges increases, further polarising the local gap region to which the charge is confined. The introduction of distance-dependent forces to the plasmon

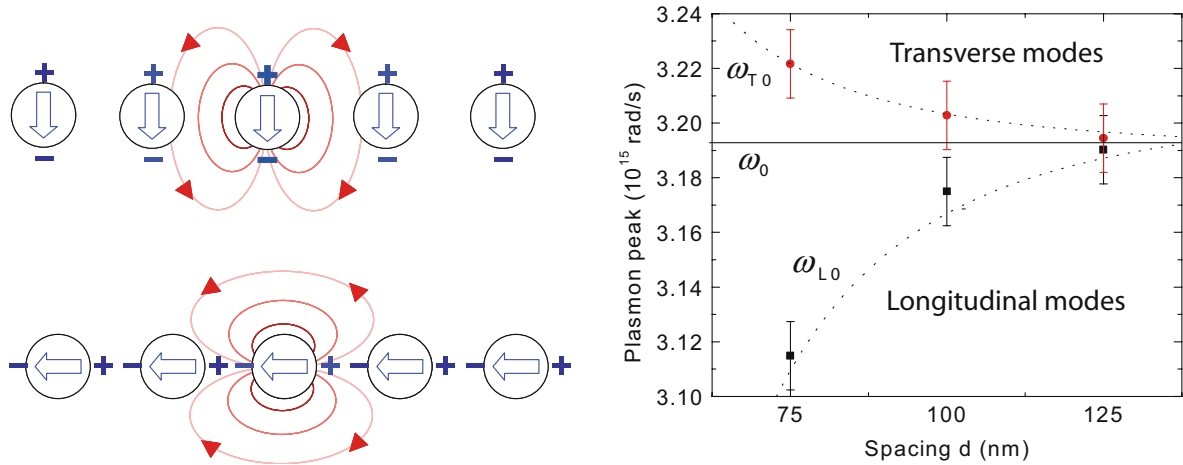


**Figure 1.7: Experimental and theoretical plasmon coupling.** Dipolar plasmons in chains of spherical AuNPs couple depending on field orientation [14] (left). Experimentally measured plasmon resonance energies in coupled AuNP chains show the gap-dependent tuning due to coupling [15] (right). The dotted line corresponds to a  $d^{-3}$  point dipole model.

oscillator shifts the resonance frequency of the individual plasmon mode from  $\omega_0$  by  $\Delta\omega$ . The coupling strength dictates the extent to which gap plasmon modes deviate from initial plasmon resonances. Since coupling is between multipolar fields, the relative orientation between the particles and the external driving field is important to determining the normal modes of oscillation, along with the phase of the driving field across the MNP system. Coupling is strongest when adjacent plasmon poles are oppositely charged.

The primary **result/effect** of gap plasmon excitation is the localisation of electric field to the dielectric medium. As stated previously, a plasmon intrinsically enhances the near-field around a metallic particle, caused by **the optically-driven** charge accumulation at the metal-dielectric interface. For the case of two interacting plasmonic particles, the forces between plasmons pulls charge more towards the region between particles. As a result charge accumulates on the metal surfaces around the gap. Much like with charged plates in a capacitor, the field in the dielectric region greatly increases. This increase in charge density from the initial plasmon field distribution further increases the near-field enhancement but on a much more confined length scale. For a strongly confined gap mode there is very little field in the metal with almost all field confined within a small lateral mode within the gap. This is known as a plasmonic "hot spot". Through this mechanism **alone** the field enhancement  $|E/E_0|$  can be increased from  $\sim 5$  to up to  $\sim 100$ . For this reason attention has shifted from individual plasmonic nanostructures to coupled systems to extract the maximum performance.<sup>10</sup>

Systems of AuNPs were studied from 2003 [15], in which the individual resonances of AuNP chains with different spacings were shown to couple and form two new modes gradually

<sup>10</sup>Is charge localisation only for the in-phase bonding modes via attraction since the other modes are from repulsion?

separating in energy with increased coupling strength (Figure 1.7). These modes are the in-phase coupled modes between particles in orthogonal polarisations. The resonance along the chain redshifts with increased coupling due to attraction between plasmons whereas the resonances perpendicular to the chain blueshift as dipolar plasmons in this orientation repel.

Interactions between plasmons appear similar to dipole-dipole interactions, which also depend on separation and relative orientation. Examples of dipole-dipole spatial interaction geometries are shown in Figure 1.8. For two parallel dipoles aligned along their axes, driven in phase, (configuration 1) the attractive coupling potential increases with decreasing separation,  $d$ , as  $V \propto p_1 p_2 d^{-3}$  [17]. For an oscillating dipole this decreases the resonant frequency. Conversely, the repulsive interaction between two parallel dipoles aligned perpendicular to their axes (configuration 3), also increasing as  $d^{-3}$ , but increases the resonant frequency. Symmetric anti-phase configurations lead to local field cancellation. Observation of such modes only become possible in non-symmetric dipole-dipole systems once a system becomes large enough that phase retardation of the driving field is significant.

For plasmons in MNPs, the coupling interaction is well approximated using the dipole-dipole model [15, 18–20], however the restoring force within the particles also contributes to the potential and goes as the volume  $D^3$ . The interaction energy between two plasmons therefore goes as  $(d/D)^{-3}$ . Since the gap size,  $s = d - D$ , is the defining feature of a plasmonic dimer, relations are often expressed in the quantity  $(s/D) = (d/D) - 1$  rather than using the centre of mass separation. The resonant wavelength shift due to coupling can then be described using a plasmon ruler equation [21, 22],

$$\frac{\Delta\lambda}{\lambda_0} = a \exp\left(-\frac{(s/D)}{\tau}\right), \quad (1.42)$$

where  $a$  is the couple strength and  $\tau$  is a decay constant. The exponential decay is considered to be approximately equivalent to the  $(s/D)^{-3}$  behaviour, which is expressed in terms of shape and size parameters,  $\Lambda$  and  $\gamma$ , as,

$$\frac{\Delta\lambda}{\lambda_0} = \frac{1}{12\Lambda(s/D + 1)^3 - (1 - \gamma)}. \quad (1.43)$$

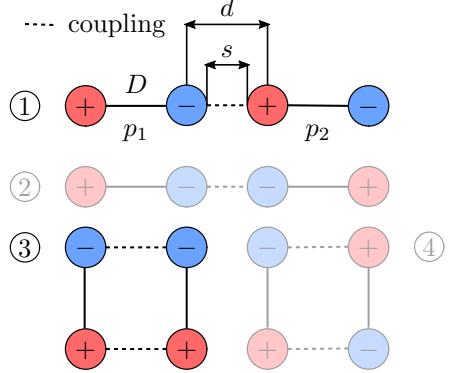


**Figure 1.8: Diagram of dipole interactions.** Dipoles have length  $D$ . The distance between dipoles is  $d$  with an edge-to-edge separation  $s$ . Configurations 1 and 3 are comparable with plasmon coupling as a result of sub-wavelength structures being driven by a single external light field. Configurations 2 and 4 are generally unphysical without significantly increasing the system size.

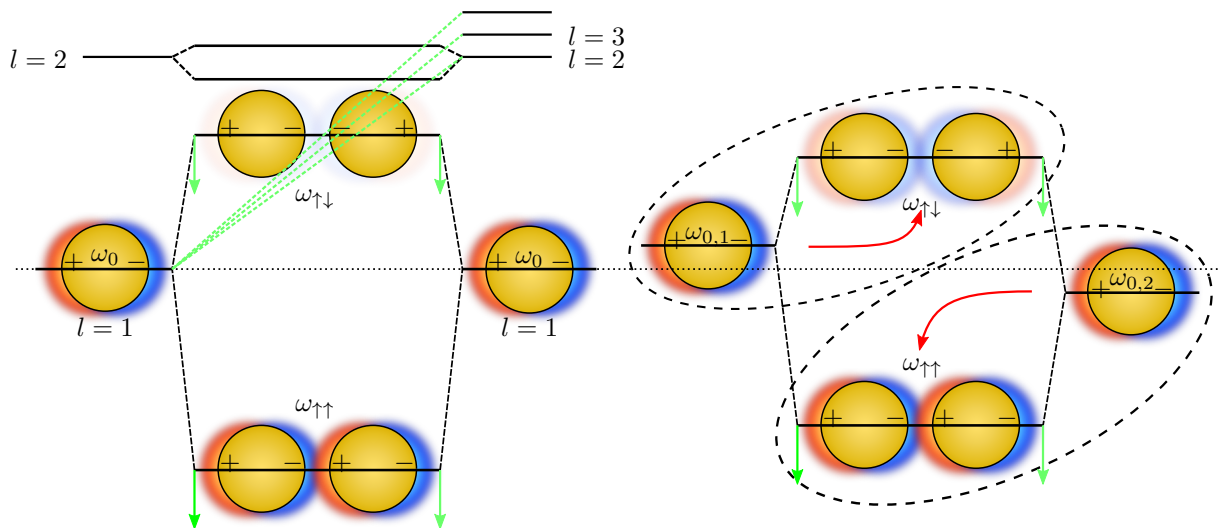


**Figure 1.9: Diagram of plasmon hybridisation between coupled plasmons in a nanoparticle dimer.** Plasmons are coupled along the dimer axis. Coupling leads to bonding and anti-bonding modes for each set of interacting  $l$  modes. Interaction with higher order  $l$  modes lowers the overall energy of lower order coupled modes (green lines). Only the bonding ( $\omega_{\uparrow\uparrow}$ ) mode in the symmetric (homo-)dimer has a net dipole moment and is therefore observable. Cancellation of the net dipole moment means the anti-bonding ( $\omega_{\downarrow\downarrow}$ ) mode remains optically dark. On the contrary, asymmetry in a (hetero-)dimer means both modes stay bright with the lower and higher energy individual modes forming the bonding and anti-bonding hybridised modes, respectively. This diagram is adapted from [23].

In recent years this relation still shows good agreement with experimental data [1] but the approach remains limited to describing only dipolar modes in simple geometries.

A slightly more complex model explaining the formation and behaviour of coupled modes was developed between 2003 and 2004. Plasmon hybridisation describes the plasmon resonances of a complex particle geometry by deconstructed it into two simpler geometries [24, 25]. This is done in analogy with the ideas underpinning molecular orbital hybridisation and the hybridisation of quantum energy states. Using this logic, the theory equally describes the plasmon resonances of two coupled simple particle geometries [23] or a particle coupled with its image charge in a surface [26]. The multipolar modes of the individual dimer particles split in energy into two hybridised modes representing the bonding (in-phase) and anti-bonding (anti-phase) pole configurations. Due to the attractive and repulsive nature of the bonding and anti-bonding configurations the coupled modes redshift and blueshift from the initial mode position, respectively. This behaviour is shown in Figure 1.9.

This model clearly shows that the bonding and anti-bonding modes have very different radiative properties. The bonding dipole exhibits a large net dipole moment due to the parallel alignment of individual dipoles, whereas the anti-parallel aligned anti-bonding mode has no net dipole. As a result, the bonding mode strongly couples with light whereas the anti-bonding mode remains dark. Consequently, anti-bonding modes can be referred to as

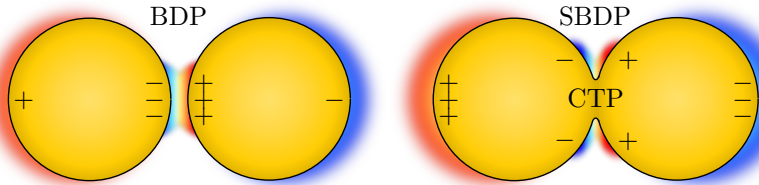


**Figure 1.10: Diagram showing the emergence of charge transfer and screened bonding (crevice) plasmons on geometrical contact in a nanoparticle dimer.** The field generated by the bonding dimer plasmon (BDP) is screened from the gap by the conductive contact, forcing capacitive coupling to the crevice gap in the form of the screened bonding dimer plasmon (SBDP). The dominant charge oscillation is then the charge transfer plasmon (CTP) through the conductive bridge and across the whole structure.

dark modes. They only become visible once a net dipole moment becomes possible, either through asymmetry of the dimer particles (difference material, size or shape) or once dimer particles become large enough that phase retardation can vary the relative dipole amplitudes.

Hybridisation between two  $l = i$  modes is also influenced by the presence of other modes of  $l \neq i$ , as is shown by the second set of dashed lines in Figure 1.9. For most simple dimer systems only the  $l = 1$  mode is observed, however, with small gaps or large particles, the  $l = 2$  mode becomes observable. In this case the  $l = 1$  mode undergoes an increased rate of redshifting due to interaction with the appearing  $l = 2$  mode. If the gap size becomes small enough that the bonding  $l = 2$  mode redshifts near to the anti-bonding  $l = 1$  mode, the interaction decreases the  $l = 1$  state energy to the point at which the blueshift is reversed [23]. Furthermore, should the gap size parameter  $s/D$  become even smaller, the increased axial dimer coupling strength means there is the potential to see even higher order modes. Classically, for nm-size gaps, a whole range of higher order modes is expected to exist in the gap [27]. The lateral confinement of these modes across the gap is estimated using,

$$w = \sqrt{Rs}. \quad (1.44)$$

Only the case of light driving plasmons along the dimer axis is shown in Figure 1.9. When light drives plasmons perpendicular to this axis the coupling strength is reduced and the excited plasmon poles repel each other. The bonding mode in this polarisation then blueshifts with increased coupling [28].

### 1.2.2 Charge Transfer Plasmonics

Upon geometrical contact between particles in a MNP dimer the gap becomes a conductive bridge. If its length is small and its conductivity is high such that charge can be transported between particles within half an optical cycle then charge transfer plasmons (CTPs) can form. The conductive short prevents the accumulation of surface charge on the gap-facing metallic

interfaces, reducing the capacitive coupling between plasmons. The capacitive hybridised gap modes are screened by the charge in the gap region and the modes move to the crevice. In another sense there are a finite number of electrons, each in a specific state, therefore if one electron transitions into a collective CTP oscillation then it's contribution is lost from its original capacitive mode. Theoretical calculations of this transition from bonding to charge transfer modes have been carried out [27, 29, 30] with experiments confirming the behaviour [31–33]. Mostly this work has been done using spherical MNP dimers, for both numerical and lithographic (experimental) simplicity.

Classical physics suggests that upon geometrical contact CTP modes form at lower energies than the bonding modes and blueshift as the particles continue to overlap [27]. This occurs since the separation of the poles of CTP charge distribution continually decreases, thus increasing the dipole energy. Each bonding mode has a corresponding CTP mode.<sup>11</sup> The width of the remaining screened bonding resonances increases due to conductive losses in the mode. As discussed in section 1.1.1 and shown in (1.10), a new contribution to conductivity will change the dielectric function. The real part of the conductivity  $\sigma$  sets the damping (**screening**) ( $\text{Re}[\sigma(\omega)] \rightarrow \text{Im}[\varepsilon(\mathbf{k}, \omega)]$ ), therefore broadening the plasmon resonance, whilst the imaginary part influences the position of the resonance by modifying  $\text{Re}[\varepsilon(\mathbf{k}, \omega)]$ . A larger overlap means a larger junction conductance, which, along with the geometrical changes, severely changes the optical response of the gap. The notion of a continually overlapping dimer is mostly unphysical but blueshifting modes back to those of a single isolated sphere is an obvious outcome. This behaviour has been observed experimentally by lithographically creating overlapped discs [31].

Changeover from capacitive to conductive modes occurs in two steps [29]. First the charge in the gap screens the bonding modes. This occurs for low conductances. An estimate of the conductance threshold for a gap separation  $d$  and **link/bridge** radius  $a$  is,

$$G_{\text{SBDP}} = \frac{\omega_{\text{BDP}}}{2\pi} \frac{a^2}{d}. \quad (1.45)$$

This quantity is considered independent of junction geometry and depends only on the conductivity ( $\sigma_{\text{SBDP}} = \omega_{\text{BDP}}/2\pi^2$ ). For a larger contact width or smaller gap size the threshold is increased to overcome the increased capacitive coupling. A second threshold exists for CTP formation. For a particle of radius  $R$ , this occurs at the second threshold,

$$G_{\text{CTP}} = \frac{\omega_{\text{CTP}}}{4\pi} \frac{R^2}{d}. \quad (1.46)$$

In a similar manner to screening the conductivity threshold is expressed as  $\sigma_{\text{CTP}} = (\omega_{\text{CTP}}/4\pi^2)(R/a)^2$ .

---

<sup>11</sup>For a spherical MNP dimer with bonding hybridised dipolar (BDP) and quadrupolar (BQP) modes the corresponding CTP modes are typically labelled as CTP and CTP'.

Unlike screening, CTP formation depends on not only the conductivity but the junction geometry. The geometry factor ( $R/a$ ) represents the ratio between the total charge in the particle and that which can pass through the gap at fixed conductivity. Having a large conductivity means the junction does not have to be as wide relative to the particle size to accommodate sufficient charge flow to maintain a CTP mode. It is typically difficult to experimentally correlate these two behaviours as the screened bonding plasmons and CTPs are usually separated by a frequency gap larger than the measurable bandwidth of the spectrometer used.

A distinction can be made between systems in which the conductive gap medium is a fixed spacer material whose conductivity can effectively be changed and systems in which the junction has the same conductivity as the metal nanoparticles (approaching nanoparticles) where geometrical changes are the cause for charge transfer phenomena. Reduction of the gap separation leading to eventual overlap In other instances the gap size has been experimentally fixed, typically using molecules which have a finite conductivity. Connecting AuNPs separated by 0.9 nm together with Au bridges using ultrafast laser pulses showed that CTPs form resonances in the NIR, which blueshift with increasing width/conductance [30, 32]. Longer linked chains consisting of small particles showed more blueshifted CTP resonances than shorter chains of larger particles. Varying the gap conductance using fractional mixing of partially conductive molecules with similarly structured insulating molecules has shown screening and blueshifting of the BDP mode and the emergence of a CTP' mode [33]. In this instance the geometry is fixed and system is therefore conductivity limited. The threshold for this behaviour is estimated as  $1G_0$ .

### 1.2.3 The Optical Response of Plasmonic Dimers

The full separation-dependent optical response of a plasmonic dimer can be numerically calculated to demonstrate the behaviour of coupled plasmons as the dimer transitions from a non-interacting state through to geometrical contact and eventual overlap of particles [27, 34]. The lowest order modes in the individual particles redshift and increase in intensity as the separation decreases. Once the gap size becomes even smaller higher order modes appear and redshift. As the higher order modes become more intense scattering from the lowest order modes decreases, despite the field enhancement increasing. These plasmons have become so confined to the gap that they no longer couple with the far-field. This summarises the classical picture of plasmon coupling (Figure 1.11a,b).

The classical picture description breaks down under two conditions - either the particles become sufficiently small that quantum non-locality and non-local effects (finite, non-negligible electron wavefunction spill-out from the particle) become important or the gap size decreases to scales on which quantum tunnelling can no longer be ignored. The onset of quantum tunnelling means charge is transported across the gap without requiring geometrical contact.

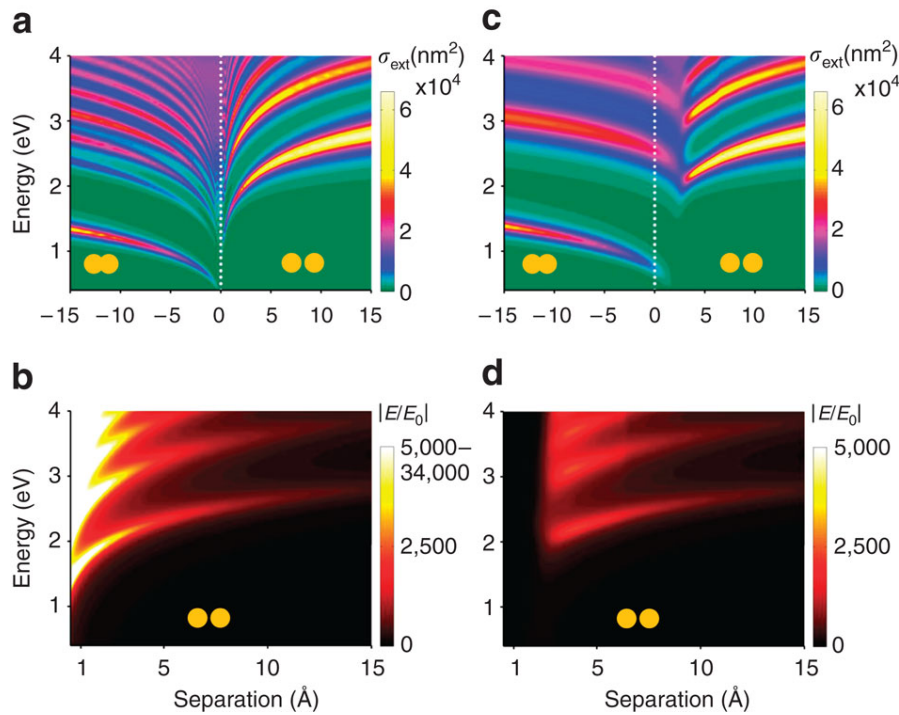


**Figure 1.11: Numerical calculated extinction cross-section and field enhancement of a spherical AuNP dimer as a function of gap separation [34].** The classical approach (left), valid for separations greater than  $\sim 5 \text{ \AA}$ , shows many modes redshifting into a singularity on geometrical contact, followed by blueshifting CTP modes as the particles overlap. Introduction of an effective (conductive) gap medium to emulate the effects of quantum tunnelling (quantum corrected model, right) demonstrate the early onset of screening and CTP formation prior to geometrical contact. Figure taken from [34].

The effects of quantum tunnelling were first predicted in small ( $R < 2 \text{ nm}$ ) Na NPs using full quantum mechanical time-dependent density functional theory (DFT) calculations [35]. Since these calculations consider the behaviour of each electron, they are limited in complexity to small systems containing less than 2000 electrons.

Tunnelling effects in larger metallic nanostructures are predicted by the quantum corrected model (QCM), a classical model which uses an effective gap dielectric function that takes into account quantum effects [34]. Electron tunnelling is accounted for using pre-calculated conductance parameters as a function of separation from DFT calculations. For large surfaces and small gaps the integrated contribution to conductance from tunnelling across the gap is enough to initially screen the bonding plasmons followed by the formation of CTPs (Figure 1.11c,d). Screening leads to strong attenuation of the field enhancement in the gap. The lack of modes present when considering quantum effects is a result of electron tunnelling smoothing the effective junction surface. It should be noted that whilst the bonding mode appears to blueshift as a result of screening reducing the capacitive coupling, simulations suggest that the blueshifting resonance is a higher order CTP excitation.

Experimental evidence of quantum tunnelling influencing plasmon coupling has been ob-

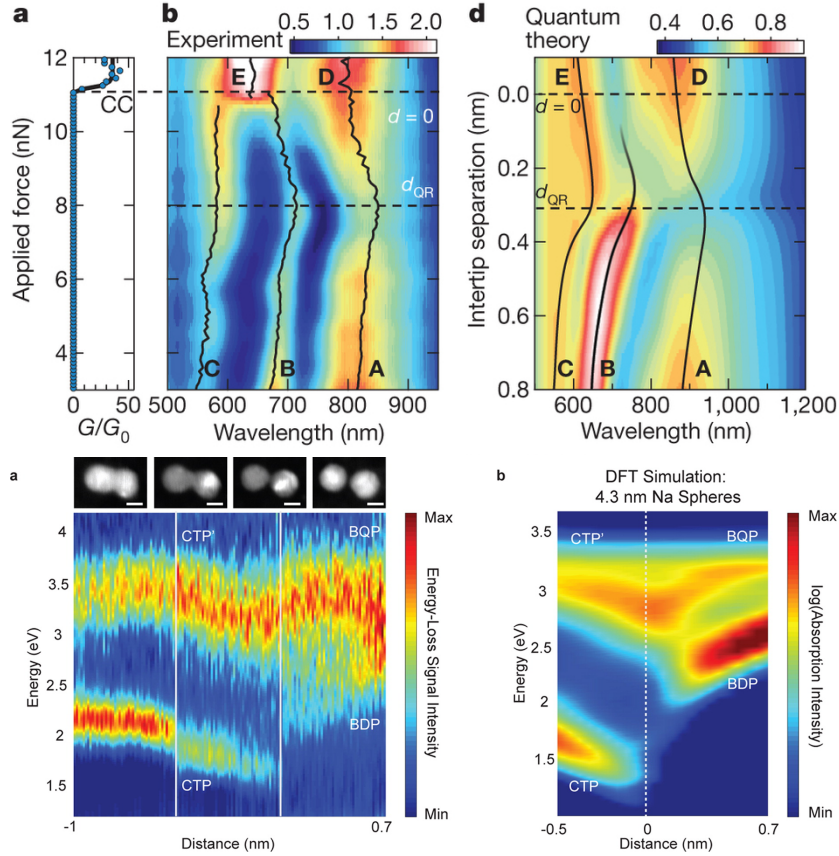


**Figure 1.12:** Examples of experimental measurements of the effect of quantum tunnelling on plasmonic gap systems through direct monitoring of the plasmon resonances. (top) Supercontinuum dark-field scattering measurements of two 300 nm diameter spherical Au tips in a dimer configuration with reducing separation, transitioning below 1 nm and into the quantum regime [36]. (bottom) EELS measurements of 10 nm AgNPs being induced closer together by the electron beam [37].

served using both optical spectroscopy [36, 38, 39], EELS [37], SERS [39], photoluminescence [40] and third-harmonic generation measurements [41]. First measurements were made using optical scattering from a dynamic spherically-tipped Au AFM probe dimer, with simulated spectra using the QCM (Figure 1.12) [36]. Plasmon modes are shown to blueshift upon decreasing past a critical separation. Scattering spectra qualitatively agreed with the QCM, with discrepancies attributed to difficulty in simulating an extended dual tip geometry. Better agreement with theory was found in EELS measurements on simpler 10 nm AgNP dimers, brought together under the influence of the electron beam (Figure 1.12) [37]. EELS agreed very well with DFT calculations. Alkanedithiol molecules of various lengths have also been used to discretely tune the gap separation of AuNP dimers [38]. In this case, blueshifting and attenuation of the BDP, as well as a measured increase in its width, is measured with molecules smaller than pentanedithiol. Similar results are found when using intercalating surface-assembled monolayers (SAMs) [42]. Further measurements on sub-nm plasmonic gaps

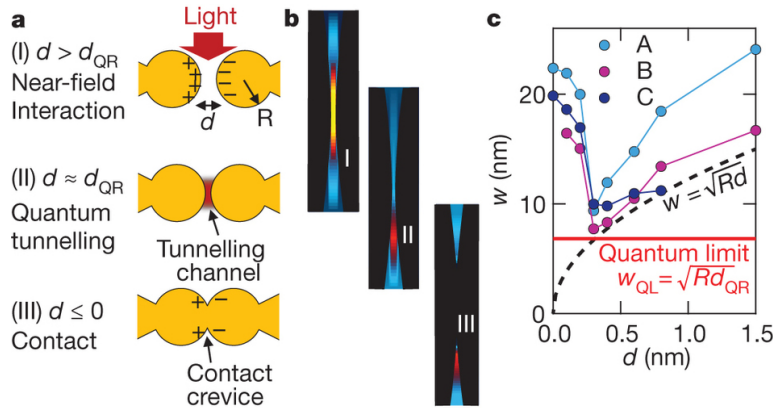


**Figure 1.13: Plasmon mode distributions in the quantum regime.** Diagram showing the different regimes of plasmonic interaction, taken from [36]. The onset of a tunnelling current pinches of the electric field in the gap via screening/conductive losses prior to conductive contact, which shows a similar expulsion of field from the gap.

have also shown changes attributed to quantum tunnelling, though inferred from properties depending on the gap field enhancement as opposed to direct monitoring of the plasmon resonances. A decrease in signal intensity in both the SERS peaks [39] and photoluminescence [40] are signatures of quantum tunnelling screening the coupled plasmon field.

Interestingly, qualitative (and to some extent quantitative) agreement between QCM calculations and full quantum calculations suggest that the quantum nature of the system is of little importance. Despite only using a classical, resistive gap with conductances given by values characteristic of electron tunnelling, the effect of electron tunnelling on gap plasmons is accurately replicated. This implies that the effects on the plasmons, despite the quantum nature of electron tunnelling, depends only on the amount of charge transfer and not the mechanism by which it occurs. This links together work done using particle positioning [36, 37] with studies of interacting plasmonic system coupled with molecular linkers [33, 38, 42].

Quantum tunnelling still remains an interesting case, however, since it is a form of conduction that is unavoidable once system sizes decrease below 0.5 nm. This is why its pinch-off point, the point at which the electric field in the gap is expelled, is described as the quantum limit to plasmon confinement [36]. It is for this reason why it is important to fully understand the relations between plasmonic hot-spots and sites of (quantum) charge transfer.

Although charge transfer effects have been shown in previous reports by varying the conductivity of a fixed gap, there has yet to be a report showing the optical response of a dynamic dimer structure correlated with its electronic response. It is the aim of this project to successfully demonstrate and explain the possible ways in which electrical and optical plasmonic phenomena **intertwine/become entangled** using a dual plasmonic nano-tip dimer. So far plasmons in planar and **spherical/spheroidal** geometries have been discussed, however many other geometries of metallic nanostructure support plasmons. Tips are one such geometry, currently

receiving significant attention, that have been shown to support both SPPs and LSPs. In order to use nano-tips in determining the effects of quantum tunnelling on plasmonics, their supported plasmons must first be understood.

### 1.3 Plasmons in Tips

Significant efforts have been made to advance surface characterisation on the nm-scale by developing new optical tools and integrating optics into existing nanoscale topological measurements. Metallic tips were therefore investigated due to the widespread use of scanning probe microscopies (SPMs), such as atomic force microscopy (AFM), and scanning tunnelling microscopy (STM). The similarity in size between metallic nanostructures and the small apex of tips initially suggested that visible plasmons would be expected, enabling resonant near-field enhancement. Prior to any spectral characterisation studies to understand the near-field response, tips were applied in combined SPM-optical microscopes to achieve sub-wavelength localisation and enhancement of optical signals. As the next logical step from surface-enhanced Raman scattering (SERS) and scanning near-field optical microscopy (SNOM), the sharp apex of tips were exploited to develop the spin-off techniques of tip-enhanced Raman scattering (TERS) [43–46] and apertureless/scattering scanning near-field optical microscopy (a-SNOM/s-SNOM) [47–52]. These are also known collectively as tip-enhanced near-field optical microscopy (TENOM).<sup>12</sup>

The concept for TENOM was first proposed in 1985 [53] but it was not until 2000 that the first reported uses of tips for enhancing Raman spectroscopy emerged [43–46]. Two of the initial measurements suggested the overall Raman enhancement has a *lower limit* of  $10^4$  [43, 44], hence a field enhancement of order 10, whereas a third demonstrated that a single tip apex has the equivalent enhancement of the sum of many SERS hotspots on a Ag island film [45]. All measurements were carried out in inverted microscopes with either an AFM [43–45] or STM [46] setup mounted on top. Near-field evanescent wave coupling using  $NA > 1$  resulted in a field enhancement of 80 [45]. Since then field enhancements of up to  $10^7$ – $10^9$  have been measured [].

TENOM is ideally classified as a local excitation approach as opposed to a local scattering approach [57], though the two approaches are not independent. In the tip scattering approach the non-radiative near-field, comprised of evanescent waves, is perturbed by the presence of the tip, leading to scattering into the far-field (**same frequency as illumination but lower  $k$** ). In the tip excitation approach the tip is resonantly excited to induce a large local near-field enhancement and used as a sub-diffraction-limited light source, from which localised scattering

---

<sup>12</sup>These are also sometimes known as field-enhancing near-field optical microscopy (FENOM) since apertured techniques do not necessarily exploit plasmonic enhancement as much.

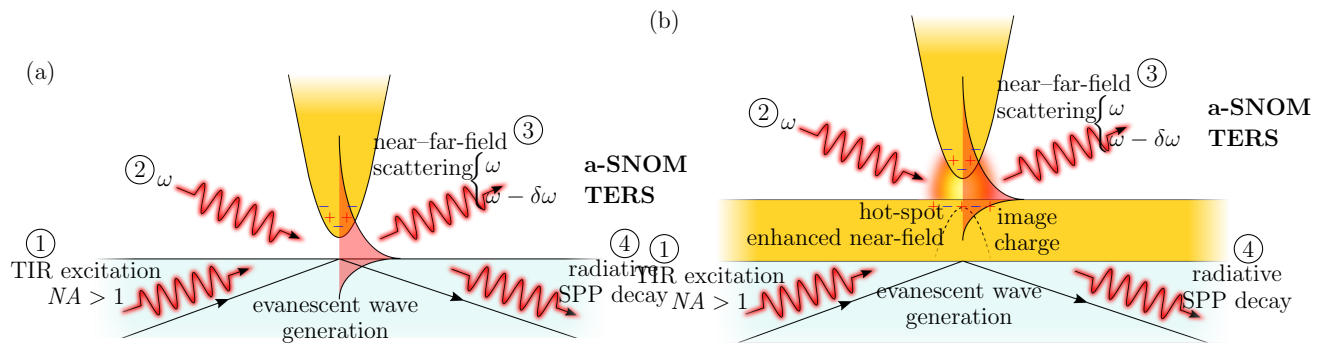


**Figure 1.14: Concepts of TENOM.** Tips can perturb evanescent surface waves and scatter them into the far-field (1 → 3) [54, 55]. Photons illuminating a tip-sample junction can induce a hot-spot, which scatters light into the far-field (2 → 3). SPPs coupled onto a planar metal surface (via a tip) can radiatively decay into  $NA > 1$  (1 → 4) [56]. Mechanism (2 → 4) has not been attempted.

can be extracted. This process can be much more efficient than the pure scattering approach but depends on the optical antennae properties of the tip (it's ability to enhance electric fields).

It was concluded that the field localisation and enhancement around the tip apex results in similar near-field measurements as in SERS and SNOM but with the advantage that the tip, unlike a stationary, fixed nanostructure, can be scanned across a sample to form an image. The resolution is limited by the size of the aperture, therefore a sharp tip with near-field enhancement has a greater resolving power than light channeled through a fibre aperture with hot spots similar in size to those in SERS. For this reason tip-based near-field techniques are widely considered to be the likely successors of static near-field techniques. However, for this to be the case, nanotips require the capability to controllably and reproducibly enhance the near-field. Understanding the electromagnetic response of metallised tips has therefore become of significant importance in recent years.

The **electromagnetic (near-field)** response of tips can be broken down into individual components that constitute the enhancement mechanism. The two main optical components are a lightning rod effect and a resonant plasmon contribution for metallic tips [58–60]. The main focus of current tip work is to tune and optimise the plasmonic component, however progress in sharpening tips has led to increases in the lightning rod component. Both of these components are important to consider to understand and control the tip near-field. Regardless of plasmonic behaviour, metallic tips intrinsically exhibit a lightning rod effect, instilling a non-resonant component of near-field enhancement under the application of an applied field. From the definition of the electric field  $\mathbf{E}(\mathbf{r}) = -\nabla\phi(\mathbf{r})$  it becomes apparent that the electric field is strongly dependent on geometry with field lines perpendicular to the equipotential conductor surface. The more curved a surface, the more compressed the field lines become around its surface due to accumulation of surface charge. This can be described by  $E = \sigma/\epsilon_0$  where  $\sigma = q/4\pi r^2$  and  $r$  is the radius of curvature. Since  $E \propto 1/r^2$  the electric field is larger

in regions of smaller curvature. This effect is shown using a simple sharp tip model in Figure 1.15. Even without a plasmonic component sharp tips provide a promising platform for localised near-field enhancement.

The expected plasmonic component arises from the curvature of the metal-dielectric interface at the tip apex. This allows for either the excitation SPPs are the apex or for SPPs propagating towards the apex to localise due to **adiabatic nanofocussing** [6]. The first direct observation of plasmons in tips was in 2005. Scattering of evanescent waves at the surface of a prism by a tip was used to measure the near-field response in Au tips [54]. The 600–800 nm spectral resonance present in Au, but not W, was attributed to excitation of SPPs at the tip apex. Further independent measurements of evanescent field scattering showed similar results [55]. ~75–100 nm shifts were observed between Ag and Au tips with a  $\text{Si}_3\text{N}_4$  base tip redshifting the resonances ~30 nm compared with coated W tips with TERS measurements suggesting that enhancement correlated with the position of the spectral resonance.

LSP excitation proves more difficult due to the extended size of the typical tip structure (~20  $\mu\text{m}$ ). Simulations of shorter tip geometries show visible to NIR LSP resonances, however these redshift and diminish with increasing tip length [59, 61]. It's for this reason that the standard metallic tip geometry makes for a poor optical antenna. **To date, despite these measurements, there is little work done to understand the optical response of tips and to characterise tips before applying them for near-field enhancement.**

Since initial investigations, tip-based systems have been designed in two configurations: the side-illumination configuration and the bottom-illumination configuration. Both configurations are shown in Figure 1.16. The specific design of a TENOM microscope is important as it defines the collection and, more importantly, excitation geometries for the tip. Side-illumination has been used successfully in a number of cases [55, 63, 64] but suffers generally from far-field scattering overshadowing the near-field scatter. This requires more complex optical geometries to fix, such as using polarisation-resolved approaches. The dominant microscope design is the bottom-illumination configuration using a  $NA > 1$  objective to illuminate the

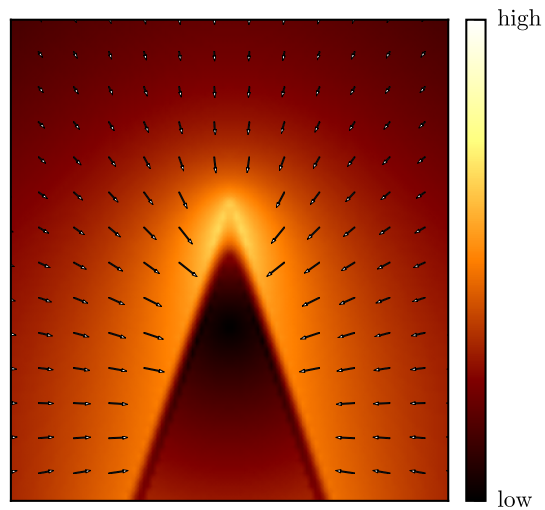


**Figure 1.15:** Calculated magnitude of the electric field around a tip showing the lightning rod effect. Compression of the field lines around the sharp corner of an equipotential surface leads to a localised, non-resonant field enhancement.<sup>a</sup>

<sup>a</sup>Poisson's/Laplace's equation is solved for a tip structured electrode with a surface charge distribution separated by some distance from a planar metal counter electrode of the opposite surface charge.

tip evanescently using a mask in  $k$ -space. Masks are similar to regular dark-field microscopy except that only  $NA > 1$  light is transmitted. This approach means minimal scattering background due to total internal reflection (TIR) of the incident light with only near-field scattering collected through the  $NA < 1$  aperture. While many use this single objective system [65–69] others use a secondary low-NA side-collection objective [70]. Bottom-illumination has the advantage that its evanescent wave illumination has the capability to couple to surface plasmons in both the sample and the tip once it is within the near-field. At this point coupling between a metallic tip and metallic sample can also occur, forming a hot spot. The disadvantage of using bottom-illumination is that it requires transparent samples (or thin enough to transmit some light) mounted onto a reflective, planar surface, which is not always possible.

### 1.3.1 Challenges associated with Tip-based Near-Field Microscopy

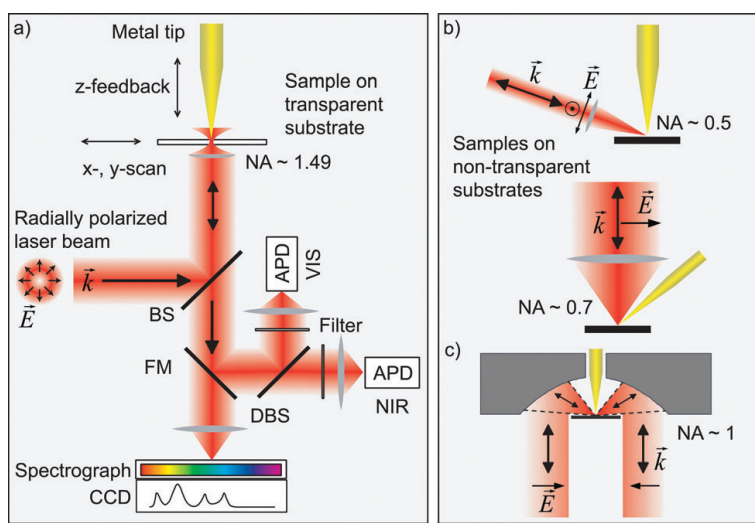


**Figure 1.16:** Typical optical geometries found in TENOM experiments [62]. The most prominent system is the bottom-illumination/back-illumination configuration utilising high-NA objectives. The other main geometry is the side-illumination configuration.

Since the initial measurements of tip plasmons, techniques such as TERS and a-SNOM have become widespread and generally accepted. However, they are currently not reliable enough to be considered as a standard technique. The current challenges with tip-based techniques include improving the reproducibility of the near-field enhancement between tips [69, 72], successful modelling of the optical processes and understanding the optical response of tips [6]. Lack of control of the tip near-field is both a result of the irreproducibility of the tip geometry and the lesser understanding of the optical processes, leading to large variations between reported field enhancements. A selection of TERS field enhancements and contrasts from reports between 2000 and 2011 showing the large variability are shown in Figure 1.17.

It is clear that sharper STM tips result in a larger field enhancement than AFM tips. Comparative studies have also shown similar trends [73]. This is most likely evidence that the lightning rod effect plays a significant role in the near-field enhancement process. Intuition suggests that the sharper profile of solid metallic STM tips means a larger lightning rod component compared with metallised AFM tips. Studies have also shown that large enhancement

**Figure 1.17:** Comparison of TERS field enhancements and contrasts reported between 2000 and 2011 [71]. STM tips, likely due to their increased sharpness, outperform AFM tips. Ag tips outperform Au tips. Larger enhancements are observed in systems where there is an underlying thin, noble metallic film. Statistical correlations still remain somewhat weak, showing the current variability in TERS experiments, attributed to irreproducibility of enhancing tips.

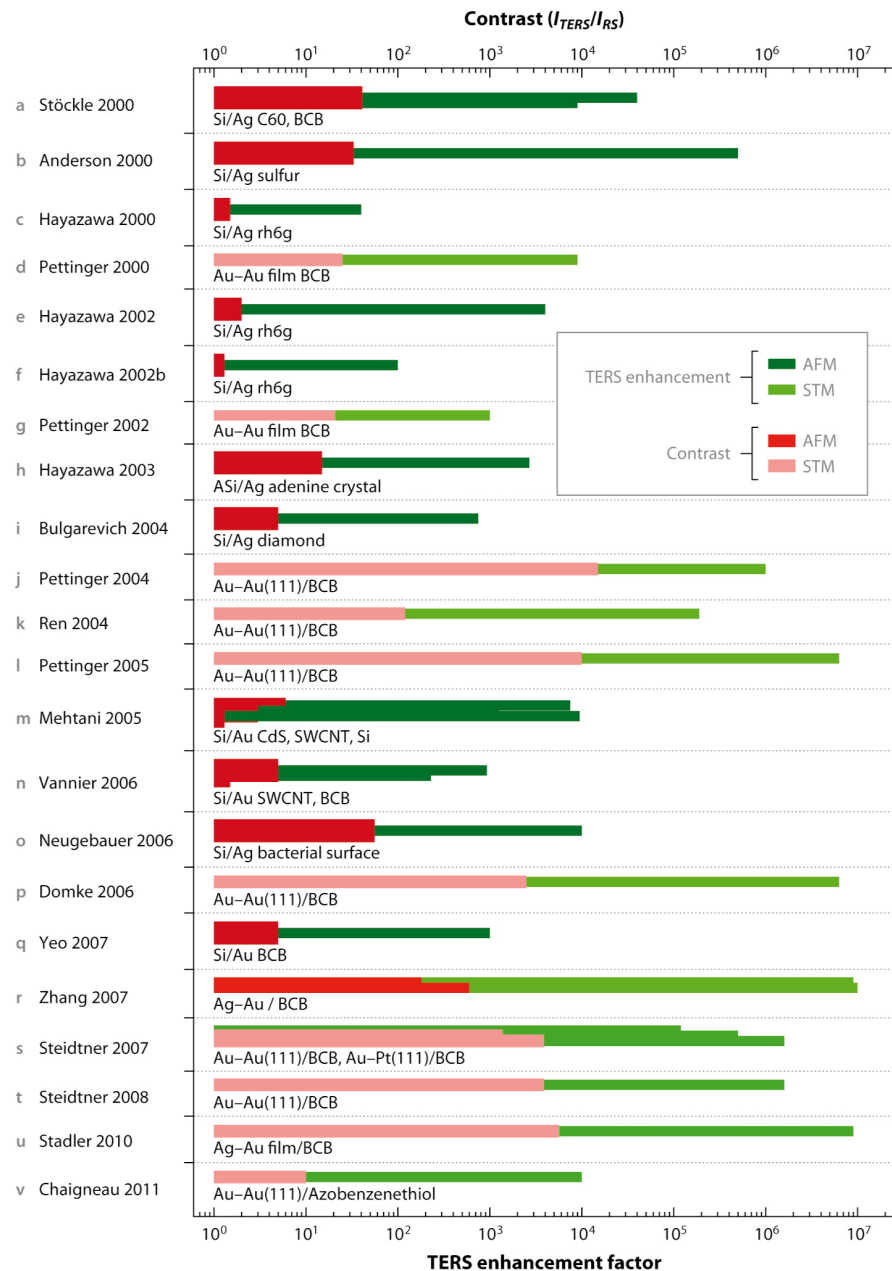


**Figure 1.18:** SEM images of metallised tips showing the granular texture and apex sharpness. (a)[65, 75].

factors can be reported due to non-plasmonic artefacts caused by the tip shaft [74]. These artefacts can be removed to recover the near-field enhancement [69] (**noting that lightning rod effect is still a near-field enhancement**), therefore the possibility for a plasmonic response is not ruled out.

Variability between similar measurements is not solely due to differences in experimental setup or a change in tip sharpness, as discussed before. A large amount of variability stems from the surface metal morphology. The plasmonic component of the tip is generally reported to originate from surface roughness that mimics the optical antenna properties of nanoparticles. Each grain of the coating can act as points at which plasmons can couple or radiate, hence a grain located at the apex can plasmonically enhance the near-field. For this reason TERS tips are typically metallised dielectric tips, coating using evaporation under similar conditions used to deposit metal islands on film [65, 75] or chemical reactions [76]. Orientation of the tip with respect to the sample has also been shown to influence the near-field enhancement [66].

As with conventional plasmonics, Ag tips generally outperform Au tips under visible light, though these claims strongly depend on the underlying tip material and the morphology of the metallic surface used in the experiment. Plasmon excitation is complicated as resonances are shifted by the refractive index of the underlying tip material. Careful consideration must be given when pairing a TERS probe with a laser. Experiments have demonstrated that matching the excitation wavelength to the plasmon resonance increases the near-field enhancement [66, 67, 75, 77]. Numerical simulations further show that resonance positions are highly sensitive to the metallic coating thickness when below the skin depth ( $\sim 40\text{ nm}$ ), suggesting some experimental variability comes from the accuracy of the metallic deposition process [61].

The previous observations all supports the hypothesis that a tip in some ways supports plasmons, which contribute to the overall near-field enhancement. However, the dependence on random depositions of rough metal is the main downfall of TERS and the more likely reason for the lack of reproducibility between measurements. Though many reports are motivated by the need to improve the reproducibility, typically via tuning the underlying tip dielectric material, very few have achieved this due to the reliance on the grain structure. [72]

Larger enhancements also occur when a thin metallic substrate films is used, suggesting formation of more localised gap plasmons.<sup>13</sup> Even between similar measurements there is a strong variability. Variations can be attributed to many factors other than the enhancement from the tip, including the tip placement, optical setup and illumination/collection geometry used. As tips are rarely characterised there is little traceability between measurements from which to determine any relevant cause for difference. However, in this time, further experi-

---

<sup>13</sup>Should probably look into those references and append wavelengths.

ments have been carried out to study the plasmonic nature of noble metal tips to understand the near-field around an illuminated tip. Theory has also been developing to complement experiments and successfully model and disentangle the optical response of tip systems.

Gap modes may form in tip systems where the underlying sample substrate is metallic. Coupling between a tip and excited SPPs on the planar metallic substrate yields a hot spot with potentially large enhancements. This is often exploited and, as a result, the Raman enhancement has been shown to rise to the order of  $10^7$  when illumination is on resonance with the gap mode[70].

Since tips are typically illuminated with single wavelength light it becomes difficult to discern plasmonic features hidden in the collected light. Electrical excitation of plasmons has been used to circumvent this limitation after the observation of light generation between a STM tip and a metal surface [71]. Electrical excitation functions to both remove the background light from the illumination source and also can excite any modes with frequencies  $\nu$  satisfying  $h\nu \leq eV$ , where  $V$  is the surface voltage of the STM. Using tunnelling current excitation, light has been observed from both the tip-air-metal surface gap [72] and the interface between the metal surface and its underlying dielectric substrate [56]. Light detected from metal-glass interfaces is leakage radiation from SPPs on the metal-air interface as the SPP dispersion crosses the light line ( $k_{SPP} = k_{glass} = nk_{air}$ , see Figure. 1.4, chapter 1) [56]. Since light cannot leak from SPPs at the metal-air interface the detected light must be from gap plasmons between the tip apex and the surface [73]. It is thought that 95% of the emission is due to SPP excitation rather than LSP excitation [56].

[78]

### 1.3.2 Experimental Considerations for Tip-Enhanced Near-Field Measurements

While it is accepted that tip-based field enhancement is a working phenomenon, many are content to apply this knowledge and focus on improving the equipment and imaging procedures in order to maximise the quality of near-field images. Mostly this is in regard to the removal of background scatter. The use of lock-in detection of a vibrating AFM cantilever has been successful in isolating the signal when the tip is near to the sample compared with the general background scatter of the tip and sample in the laser focus [74]. Other solutions are to remove the background scatter altogether by fabricating tips with side gratings in order to couple light into propagating SPPs that focus and reradiate at the apex to form a nanoscale light source [75]. These reports also demonstrate that a sharp apex acts as a defect point at which SPPs can outcouple to photons. By reciprocity it also means that near-field light can also excite SPPs at the apex which can propagate away from the apex.

For this reason a selection of techniques are desired to optically characterise tips prior to

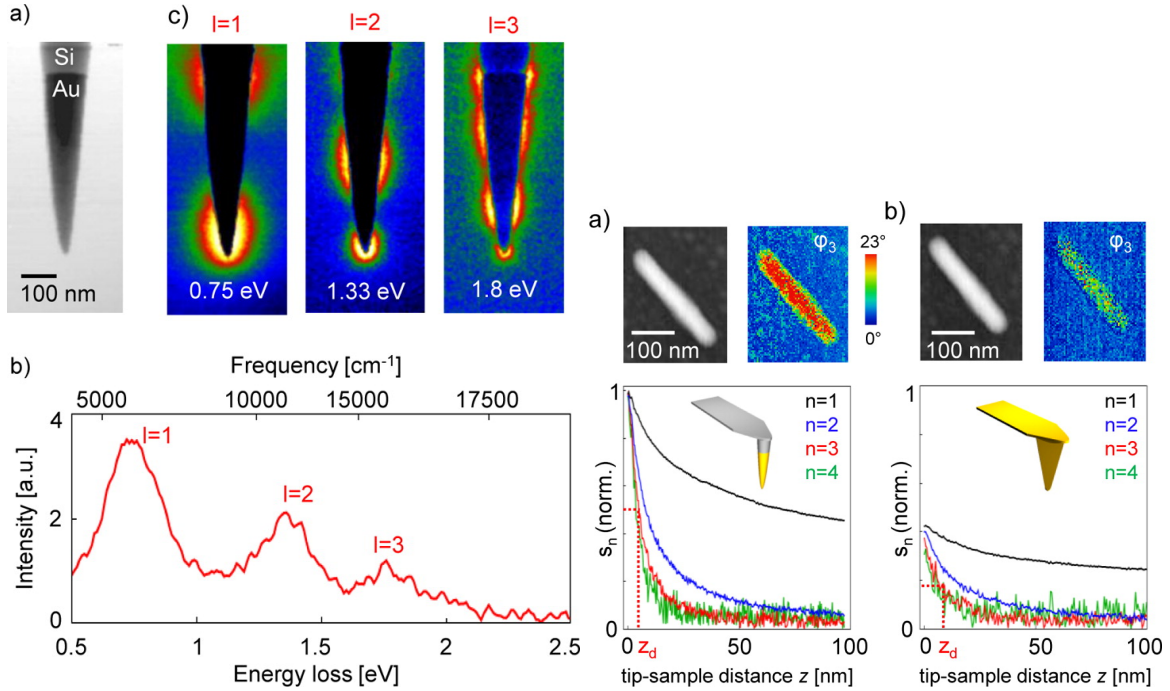


**Figure 1.19: Comparison between standard Au and nano-antenna AFM tips [82].** Nano-antenna tips comprise a Au nanotip on a FIB-cut Si AFM tip. EELS spectra show multipolar rod LSP plasmon modes and scattering measurements demonstrate that nano-antenna tips outperform standard metallised tips.

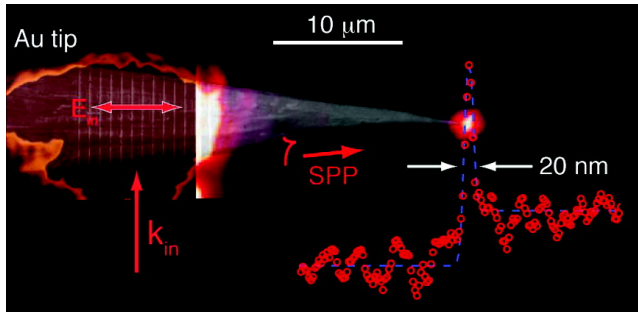
use.

### 1.3.3 Optical Antenna Tips

The mode mismatch caused by the size difference between diffraction-limited light and the nm-scale results in a 3–4 order magnitude coupling efficiency loss [79]. As described previously, a plasmon acts as an optical antenna. A good optical antenna has the ability to effectively modify the density of electromagnetic states such that the far-field radiation impedance is efficiently matched with the impedance of a near-field evanescent mode and vice versa [57, 80]. The antenna opens up scattering pathways that connect wave states ( $k$ -vectors) by creating new intermediate states, thus enabling local evanescent waves to find a pathway to radiative emission. Metallic tips, in their standard form, are not particularly good optical antennae [59]. **The lack of radiative lower order multipolar resonances greatly diminishes the radiative cross section [81].** To improve transmission efficiency, standard sharp, pointed tips and their surrounding structures can be modified or nanostructured to introduce such intermediary states which effectively couple the far-field to the near-field [62].

Designs in which the tip is removed and replaced with a planar bow-tie antenna [83] or nano-cone [84] have demonstrated improved field enhancements due to resonant excitation of a LSP mode in the modified apex structure. Such modification and attachment is typically

**Figure 1.20: A grating-coupled Nano-tip light source.** Imprinting a grating onto the side of an AFM tip allows far-field excitation of SPPs, which focus and localise at the apex, emitting nanoscale light [85]. This can be used to circumvent far-field background scatter at the apex for improved near-field measurements [13, 79]. Emission mechanics are similar to electrical excitation of SPPs but no longer requires an underlying plasmonic substrate and gap coupling.



carried out using FIB machining of base AFM tip structures during electron microscopy, in which the size of the structure can be varied to tune the plasmon resonance. Investigations into the plasmons of similar nano-tip optical antennae of different lengths show that scattering from the near-field is increased by 120% when using resonant localised plasmon modes [82]. Note however that this is using a side-illumination geometry which is efficient only at targeting multi-polar antennae.

One particularly useful example of SPPs on the surface of tips and nanofocusing is illustrated by imprinting a grating onto the side of the tip [85] or by coupling to SPPs using a photonic crystal waveguide [86]. Usually near-field evanescent wave coupling is required to excite SPP modes in tips, however diffraction gratings also impart momentum allowing photons to couple with surface plasmons [6]. When the grating is illuminated excited SPPs propagate towards the apex. Only a single mode can exist at the apex, which localises and re-emits as a nanoscale light source (Figure 1.20). As with electrical excitation experiments, this clearly demonstrates that SPPs will radiate into the far-field at the apex of a sharp tip. Unlike electrical excitation, however, plasmonic gap coupling is not required to scatter SPP radiation. A disadvantage is that this technique is only shown as viable for  $\lambda_{SPP} \geq 800$  nm.

Although nanostructuring has been shown to improve the optical response of tip structures the current techniques, mainly based on FIB techniques, are costly and time consuming. Part of this project is dedicated to the development of a simple method for producing plasmonic antenna tips.

### 1.3.4 Theoretical Modelling of Tip Nanophotonics: Understanding the Near-Field Response

Theoretical analysis and modelling of tip structures is difficult. The main difficulty comes from the range of length scales of tip structures. The apex diameters of tips can easily be below 50 nm while the overall tip length can extend to over 20  $\mu\text{m}$  with various feature sizes in between.

An early, and ultimately dissatisfying, model considered the apex radius and material composition as the only important parameters, approximating the apex as a sphere [1]. The fundamental issue with this approach is that a sphere has a back surface on which poles of lower order LSP modes exist. Predictions of spectra therefore include antenna modes not compatible with a realistic tip geometry [1]. Later approaches used an elliptical particle to mimic the increasing sharpness of a tip [1]. In this case the polarisability is redefined as,

$$\alpha_i(\omega) = 4\pi a_1 a_2 a_3 \frac{\varepsilon(\omega) - \varepsilon_d}{3\varepsilon_d + 3L_i(\varepsilon(\omega) - \varepsilon_d)}, \quad (1.47)$$

to include the geometrical factor,

$$L_i = \frac{a_1 a_2 a_3}{2} \int_0^\infty \frac{dq}{(a_i^2 + q)\sqrt{(q + a_1^2)(q + a_2^2)(q + a_3^2)}}. \quad (1.48)$$

The resonance condition is then changed to,

$$\text{Re}[\varepsilon(\omega)] = -\frac{1 - L_i}{L_i} \varepsilon_d, \quad (1.49)$$

therefore by decreasing the geometrical factor the resonance decreases from  $-2\varepsilon_d$ . This corresponds to a decrease in the frequency and a redshifted plasmon. The longer the particle is the larger the redshift until the particle is large enough to no longer be considered plasmonic. Using this approach, strictly within the quasistatic regime, it becomes obvious why a long, sharp tip cannot sustain lower order, multipolar LSP modes that couple with the far-field.

The different length scales associated with a large tip causes issues when using modelling techniques that split a surface into a mesh grid. Around the apex a fine mesh with sub-nm grid sizes is required to accurately solve Maxwell's equations on such a small feature size, however it is not computationally feasible to use this mesh size across the whole  $\mu\text{m}$  scale structure. In many cases only the tip apex is modelled with a high resolution grid resulting in unphysical modes appearing due to SPP or LSP excitation due to actually modelling a sub- $\mu\text{m}$  scale antenna structure, like a nanoparticle [1], or even modelling the apex as a nanoparticle. Plasmons such as these are artefact of an artificially small nanostructure, caused by interference between waves propagating along a much smaller surface than is actually available or polar charge distributions that cannot exist if the length of the tip is increased due to charge cancellation by the appearance of positive ions. On the other hand, adaptive meshing can be used to take the extended tip structure into account whilst maintaining a finer grid around the apex curvature. The length of the tip, although increased, still contributes some SPP interference resulting in visible modes.

Calculations also rarely take into account the actual shape of experimental tip structures (typically created using an etching process along crystal planes), instead exploiting symmetry

to improve the calculation time by modelling the tip as a perfect cone. When the length of a more realistic tip structure is taken into account the resonant plasmon modes reduce disappear into a smooth continuum [59]. Between 200 nm length and an infinite length a tip transitions between supporting low order LSPs, then higher order LSPs, followed by only weak SPPs. LSPs are supported only when the entire tip structure is comparable in size to the focus, allowing light to drive in-phase collective oscillations of the conduction electrons. As the tip becomes larger than the focus, and hence the illumination wavelength, phase retardation occurs and higher order LSP modes dominate. Once the tip becomes larger than the focus collective oscillations are no longer possible, leaving only LSPs concentrated at the apex surface and SPPs. The SPPs form the periodic response in the field enhancement before disappearing due to increasing losses when the tip length is increased further. The field enhancement inevitably rises smoothly and non-resonantly towards the IR due to only a lightning rod effect contribution being present. In this case the rise is caused by the longer wavelengths becoming larger than the apex radius or curvature, thereby creating an apparent increase in sharpness. To this extent, Zhang *et. al.* suggest that the improvement in TERS over time is correlated with the availability of new technology to fabricate sharper metallic tips since SPPs remain weak and lossy allowing the lightning rod effect to dominate. Furthermore, Figure ??(b) shows that even a sharp tip with a 10 nm radius cannot compete with the enhancements brought on by collective LSP excitation in a broader apex.

Due to limitations in experimental fabrication processes the metallic surfaces can rarely be considered flat, with granular surfaces and atomic scale roughness considerably changing the plasmonic response [] .

Calculations of a Au tip approaching a Au surface, considering only the apex region (adaptive meshing), in the quasi-static approximation [87]. By considering only the quasistatic regime the Laplace equation can be analytically solved, simplifying the computation time and giving greater insight into the physical quantities and how they behave. However, this approach assumes a plasmon exists at the apex with no method of optical excitation other than evanescent wave coupling.

One difficulty when comparing a calculated near-field response compared with a measured far-field spectrum is distinguishing between modes which can exist but are dark and those which can couple with light, specifically considering what conditions are required for optical coupling. To this extent an antenna mode is applied to attempt to disentangle spectral modes into those which can be observed in the far-field and those which can't.

Despite the experimental drive to produce sharper tips, it has been suggested that the sharpness of tips eventually enter a regime where non-locality (quantum mechanics and electron-electron interactions) becomes important. In this regime the field enhancement is reduced and limited by nonlocal effects and localisation effects of structural surface imperfections and

sharpness are heavily reduced [88], suggesting a quantum limit to field confinement. Both the strength of the lightning rod effect and the confinement of SPPs are therefore limited, meaning that contributions from different plasmonic mechanisms is necessary to further pursue larger field enhancements with tips.

Despite using an apex-localised, quasi-static model to analytically predict the spectral response of tips and tip-sample interactions, a visible frequency plasmon resonance ( $\sim 550$  nm) is calculated for a hyperbolic tip, one which is independent of cone angle, which only affects the field enhancement, but sensitive to tip radius (redshifts with decreasing radius) and gap coupling with a planar surface [87]. As with any quasi-static model phase retardation is neglected meaning it is not possible to predict multipolar resonances. While this model shows agreement with FTDT calculations [] and early experimental measurements [54] the specific conditions required to excite the LSP are not discussed.

Experimental observations show that sharper STM tips give more enhancement than AFM tips [66, 71], suggesting that a significant component of tip enhancement is a strong contribution from the lightning rod effect. Simulations using the premise of an infinite conical tip computationally replicate this behaviour as the tip length is increased [59].

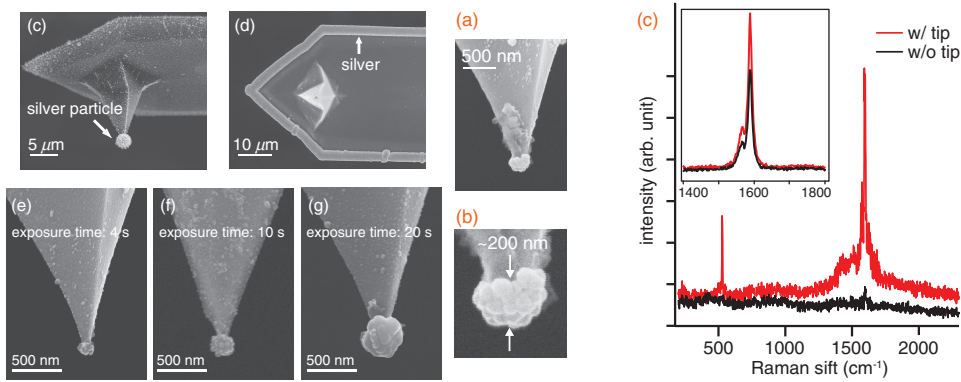
Further evidence for the lack of a plasmonic contribution comes from the comparison between metallised Au tips and Au antenna tips [82].

### 1.3.5 Plasmons in Apex-Nanostructured Tips

Recently, nanostructuring of the tip apex has been applied to tune and optimise the optical (plasmonic) properties of nanotips. By reducing the characteristic size of the apex structure, thereby giving it a new, more localised, geometry, light can be more strongly confined in more localised plasmon oscillations, hence the optical antenna properties of a nanotip can be substantially improved. The emergence of new plasmon modes unsupported by regular sharp tips then opens up new mechanisms through which light can be channelled to the nm-scale, such as direct far-field illumination.

The simplest geometry to impart onto a tip apex is a sphere. By doing so the tip gains plasmon modes similar to that of an isolated spherical nanoparticle. The specific mode depends on the method used for attachment as the base tip structure affects the plasmons. To date there have been a number of methods reported for spherically structuring a tip apex.

Non-metallic spherical tips on AFM probes have been created using methods such as vacuum-processing diamond-like carbon growth (NanoTools B-series) and AFM droplet pick-up []. These nanotips can then be made plasmonic through evaporation of a metallic coating. Other methods directly focus on structuring the apex with a solid metallic structure rather than using a post-fabrication coating. The concept of metallic spherical nanoparticle attachment has been reported numerous times over the last decade [90], beginning with the use



(a) Photochemical fabrication of (b) TERS measurements and numerical AgNP-tipped AFM probes (c) simulations of AgNP-on-Si tips.

**Figure 1.21: Photochemically fabricated AgNP-on-Si tips for TERS [89].** Field enhancement is increased  $\sim 20\times$  compared with sharp Ag tips when using 488 nm illumination with a 1.4 NA objective in an inverted microscope.

of fibres as mounting structures [91–94] and progressing onto the use of SPM tips [75, 89, 95–98]. Examples of nanotips modified with metallic spherical nanostructures are shown in Figure 1.21.

Plasmon resonances in spherical tips have been observed in the far-field [36], with coupling between plasmons used to confirm plasmonic behaviour. Furthermore a  $20\times$  increase in field enhancement has been measured when using a photochemically-fabricated spherical AgNP-on-Pt tip compared with a sharp Ag tip [89]. The increase in field enhancement also comes with an increase in **resolution/spatial localisation**.

Nanostructuring tips with other geometries has also led to an order of magnitude increase in field enhancement, attributed to LSP excitation. Electrochemical etching [99], FIB machining [100], selective deposition [101] and grafting [82] have successfully been used to create nanotips which are good optical antennae, especially when illuminated on resonance. Scattering resonances have been directly measured on a subset of these tips [100, 101] while others use the field enhancement at common laser wavelengths as a measurement of antenna quality [99].

[63, 78, 95, 102–121]

To date there has been very little work done to reliably produce and characterise the optics of spherically nanostructured tips. Furthermore, there is still work needed to similarly measure the optical response of sharp tips, comparing them directly and quantitatively with nanostructured tips. This project focusses on developing a simple method for producing plasmonic tips with understood far-field optical responses. The comparison with sharp metallic tips can then be made and plasmonic tips applied in both fundamental studies and near-field enhancement.

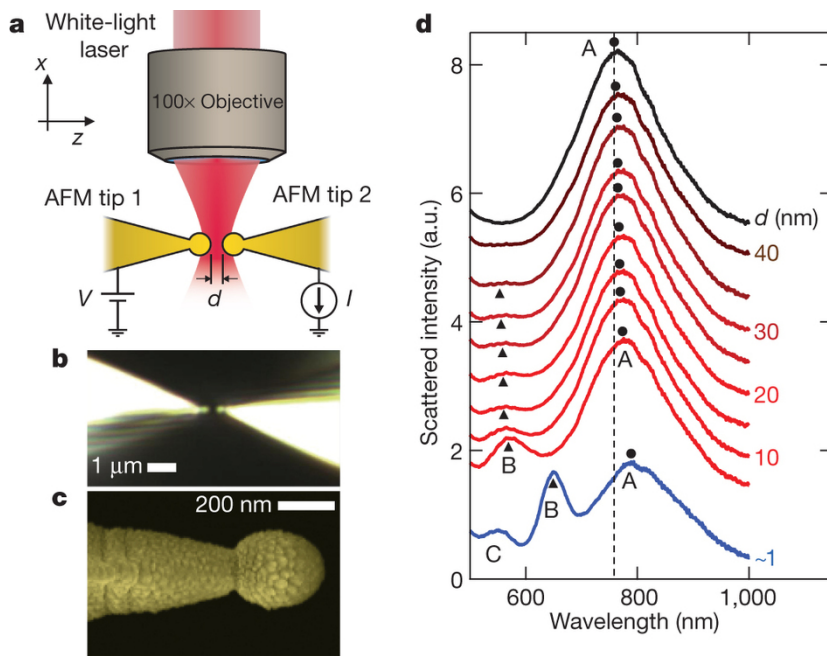


**Figure 1.22:** Experimental evidence of spherical tip plasmons and their dynamic coupling into the quantum regime of plasmonics [36]. Spherical tips are Au-coated NanoTools B150 AFM probes (150 nm radius of curvature), selected to minimise sensitivity to axial tip-tip alignment, to increase the scattered signal levels, and support higher-order plasmonic cavity modes in the visible spectrum. Resonances are far-field excited using a supercontinuum laser source in a side-illumination configuration. Separation-dependent coupling between two spherical tips confirms plasmonic behaviour.

## 1.4 Conclusions

Charge transfer effects in plasmonic systems are a phenomenon still requiring significant investigation. The influence of electron tunnelling has only been touched upon in recent years. Tips, if possessing far-field antenna plasmons, provide a useful platform for studying fundamental plasmonics in a dynamic way. Their well-developed experimental geometries for topological measurements form the basis of microscopes integrating optics and tips. By using such a setup the quantum regime of tunnelling plasmonics can be further investigated.

To date there has been no direct correlated measurements between plasmon resonances and quantum tunnelling. Tunnelling has been inferred from direct measurements of plasmon resonances without electronic measurements [36, 37] and from variables influenced by the gap field enhancement, though in some cases with electronic measurements [38, 39, 41, 42]. The effects of tunnelling, specifically the relations between screening and CTP excitation, can be better understood with correlated electrical and force measurements. By using an experimental geometry related to AFM these measurements become possible.



# References

- [1] J. C. Maxwell, Philosophical Transactions of the Royal Society of London, 459–512 (1865).
- [2] P. Drude, Annalen der Physik **306**, 566–613 (1900).
- [3] P. B. Johnson and R.-W. Christy, Physical Review B **6**, 4370 (1972).
- [4] A. Otto, Zeitschrift für Physik **216**, 398–410 (1968).
- [5] E. Kretschmann, Zeitschrift für Physik **241**, 313–324 (1971).
- [6] R. Wood, The London, Edinburgh, and Dublin Philosophical Magazine and Journal of Science **4**, 396–402 (1902).
- [7] U Fano, JOSA **31**, 213–222 (1941).
- [8] J. D. Jackson, *Classical electrodynamics* (John Wiley & Sons, 1999).
- [9] J. Mock et al., The Journal of Chemical Physics **116**, 6755–6759 (2002).
- [10] H. Kuwata et al., Applied physics letters **83**, 4625–4627 (2003).
- [11] C. F. Bohren and D. R. Huffman, *Absorption and scattering of light by small particles* (John Wiley & Sons, 2008).
- [12] G. Mie, Annalen der physik **330**, 377–445 (1908).
- [13] S. Berweger et al., The Journal of Physical Chemistry Letters **3**, 945–952 (2012).
- [14] S. A. Maier, *Plasmonics: fundamentals and applications* (Springer Science & Business Media, 2007).
- [15] S. A. Maier, P. G. Kik, and H. A. Atwater, Applied Physics Letters **81**, 1714–1716 (2002).
- [16] J. Mertens et al., Nano letters **13**, 5033–5038 (2013).
- [17] N. J. Halas et al., Chemical reviews **111**, 3913–3961 (2011).
- [18] U. Kreibig and M. Vollmer, *Optical properties of metal clusters*, Vol. 25 (Springer Berlin, 1995).
- [19] M. Gluodenis and C. A. Foss, The Journal of Physical Chemistry B **106**, 9484–9489 (2002).
- [20] W Rechberger et al., Optics Communications **220**, 137–141 (2003).
- [21] P. K. Jain, W. Huang, and M. A. El-Sayed, Nano Letters **7**, 2080–2088 (2007).
- [22] X. Ben and H. S. Park, The Journal of Physical Chemistry C **115**, 15915–15926 (2011).
- [23] P. Nordlander et al., Nano Letters **4**, 899–903 (2004).

- [24] E Prodan et al., *Science* **302**, 419–422 (2003).
- [25] E Prodan and P. Nordlander, *The Journal of chemical physics* **120**, 5444–5454 (2004).
- [26] P. Nordlander and E. Prodan, *Nano Letters* **4**, 2209–2213 (2004).
- [27] I. Romero et al., *Optics Express* **14**, 9988–9999 (2006).
- [28] L. Gunnarsson et al., *The Journal of Physical Chemistry B* **109**, 1079–1087 (2005).
- [29] O Pérez-González et al., *Nano letters* **10**, 3090–3095 (2010).
- [30] C. Tserkezis et al., *Optics express* **22**, 23851–23860 (2014).
- [31] J. B. Lassiter et al., *Nano letters* **8**, 1212–1218 (2008).
- [32] L. O. Herrmann et al., *Nature communications* **5** (2014).
- [33] F. Benz et al., *Nano letters* (2014).
- [34] R. Esteban et al., *Nature Communications* **3**, 825 (2012).
- [35] J. Zuloaga, E. Prodan, and P. Nordlander, *Nano letters* **9**, 887–891 (2009).
- [36] K. J. Savage et al., *Nature* **491**, 574–577 (2012).
- [37] J. A. Scholl et al., *Nano letters* **13**, 564–569 (2013).
- [38] H. Cha, J. H. Yoon, and S. Yoon, *ACS nano* **8**, 8554–8563 (2014).
- [39] W. Zhu and K. B. Crozier, *Nature communications* **5** (2014).
- [40] V. Kravtsov et al., *Nano letters* **14**, 5270–5275 (2014).
- [41] G. Hajisalem, M. S. Nezami, and R. Gordon, *Nano letters* **14**, 6651–6654 (2014).
- [42] S. F. Tan et al., *Science* **343**, 1496–1499 (2014).
- [43] R. M. Stöckle et al., *Chemical Physics Letters* **318**, 131–136 (2000).
- [44] M. S. Anderson, *Applied Physics Letters* **76**, 3130–3132 (2000).
- [45] N. Hayazawa et al., *Optics Communications* **183**, 333–336 (2000).
- [46] B. Pettinger et al., *Electrochemistry* **68**, 942–949 (2000).
- [47] F Zenhausern, M. O’boyle, and H. Wickramasinghe, *Applied Physics Letters* **65**, 1623–1625 (1994).
- [48] F. Zenhausern, Y Martin, and H. Wickramasinghe, *Science* **269**, 1083–1085 (1995).
- [49] R Bachelot, P Gleyzes, and A. Boccara, *Optics letters* **20**, 1924–1926 (1995).
- [50] B Knoll et al., *Applied physics letters* **70**, 2667–2669 (1997).
- [51] B Knoll and F Keilmann, *Applied Physics A: Materials Science & Processing* **66**, 477–481 (1998).
- [52] F Keilmann, B Knoll, and A Kramer, *physica status solidi (b)* **215**, 849–854 (1999).
- [53] J. Wessel, *JOSA B* **2**, 1538–1541 (1985).
- [54] C. Neacsu, G. Steudle, and M. Raschke, *Applied Physics B* **80**, 295–300 (2005).
- [55] D Mehtani et al., *Journal of Optics A: Pure and Applied Optics* **8**, S183 (2006).
- [56] T Wang et al., *Nanotechnology* **22**, 175201 (2011).

- [57] L. Novotny and S. J. Stranick, *Annu. Rev. Phys. Chem.* **57**, 303–331 (2006).
- [58] R Esteban, R Vogelgesang, and K Kern, *Nanotechnology* **17**, 475 (2006).
- [59] W. Zhang, X. Cui, and O. J. Martin, *Journal of Raman Spectroscopy* **40**, 1338–1342 (2009).
- [60] T. Schmid et al., *Angewandte Chemie International Edition* **52**, 5940–5954 (2013).
- [61] C. Huber et al., *Physical Chemistry Chemical Physics* **16**, 2289–2296 (2014).
- [62] N. Mauser and A. Hartschuh, *Chemical Society reviews* **43**, 1248–1262 (2014).
- [63] R Zhang et al., *Nature* **498**, 82–86 (2013).
- [64] H. K. Wickramasinghe et al., *ACS nano* **8**, 3421–3426 (2014).
- [65] N. Hayazawa et al., *Chemical Physics Letters* **335**, 369–374 (2001).
- [66] B.-S. Yeo et al., *Applied spectroscopy* **60**, 1142–1147 (2006).
- [67] B.-S. Yeo et al., *Analytical and bioanalytical chemistry* **387**, 2655–2662 (2007).
- [68] M. Zhang et al., *Journal of Optics* **15**, 055006 (2013).
- [69] N. Kumar, A. Rae, and D. Roy, *Applied Physics Letters* **104**, 123106 (2014).
- [70] K. Uetsuki et al., *Nanoscale* **4**, 5931–5935 (2012).
- [71] B. Pettinger et al., *Annual review of physical chemistry* **63**, 379–399 (2012).
- [72] C. Blum et al., *Journal of Raman Spectroscopy* **45**, 22–31 (2014).
- [73] M. B. Raschke and C. Lienau, *Applied Physics Letters* **83**, 5089–5091 (2003).
- [74] R Ramos and M. Gordon, *Applied Physics Letters* **100**, 213111 (2012).
- [75] N. Hayazawa, T.-a. Yano, and S. Kawata, *Journal of Raman Spectroscopy* **43**, 1177–1182 (2012).
- [76] E. Bailo and V. Deckert, *Chemical Society Reviews* **37**, 921–930 (2008).
- [77] X. Cui et al., *Optics express* **15**, 8309–8316 (2007).
- [78] A. Taguchi et al., *Optics express* **17**, 6509–6518 (2009).
- [79] S. Berweger et al., *The Journal of Physical Chemistry Letters* **1**, 3427–3432 (2010).
- [80] L. Novotny and N. Van Hulst, *Nature Photonics* **5**, 83–90 (2011).
- [81] J. Renger et al., *JOSA A* **21**, 1362–1367 (2004).
- [82] F. Huth et al., *Nano letters* **13**, 1065–1072 (2013).
- [83] A Weber-Bargioni et al., *Nanotechnology* **21**, 065306 (2010).
- [84] M. Fleischer et al., *ACS nano* **5**, 2570–2579 (2011).
- [85] C. C. Neacsu et al., *Nano letters* **10**, 592–596 (2010).
- [86] A. Bek et al., *Micron* **42**, 313–317 (2011).
- [87] N. Behr and M. B. Raschke, *The Journal of Physical Chemistry C* **112**, 3766–3773 (2008).
- [88] A. Wiener et al., *Nano letters* **12**, 3308–3314 (2012).
- [89] T. Umakoshi et al., *Applied Physics Express* **5**, 052001 (2012).

- [90] Y. Gan, *Review of scientific instruments* **78**, 081101 (2007).
- [91] T. Kalkbrenner et al., *Journal of Microscopy* **202**, 72–76 (2001).
- [92] I. Barsegova et al., *Applied Physics Letters* **81**, 3461–3463 (2002).
- [93] O Sqalli et al., *Journal of applied physics* **92**, 1078–1083 (2002).
- [94] Y. Kawata et al., *Applied physics letters* **82**, 1598–1600 (2003).
- [95] C.-G. Park et al., *B. Korean Chem. Soc* **33**, 1748–1752 (2012).
- [96] T Okamoto and I Yamaguchi, *Journal of microscopy* **202**, 100–103 (2001).
- [97] I. U. Vakarelski and K. Higashitani, *Langmuir* **22**, 2931–2934 (2006).
- [98] H.-W. Cheng et al., *Nanoscale research letters* **8**, 1–10 (2013).
- [99] S. Kharintsev et al., *Journal of Physics D: Applied Physics* **46**, 145501 (2013).
- [100] I. Maouli et al., *Applied Physics Express* **8**, 032401 (2015).
- [101] Y. Zou et al., *Applied Physics Letters* **94**, 171107 (2009).
- [102] T. Ichimura et al., *Physical review letters* **102**, 186101 (2009).
- [103] C. Schäfer et al., *Nanoscale* **5**, 7861–7866 (2013).
- [104] B. Pettinger et al., *Surface Science* **603**, 1335–1341 (2009).
- [105] S. Cherukulappurath et al., *Nano letters* **13**, 5635–5641 (2013).
- [106] Y. Yang et al., *RSC Advances* **4**, 4718–4722 (2014).
- [107] J. Steidtner and B. Pettinger, *Review of Scientific Instruments* **78**, 103104 (2007).
- [108] E. M. van Schrojenstein Lantman et al., *Nature nanotechnology* **7**, 583–586 (2012).
- [109] A. M. Angulo, C. Noguez, and G. C. Schatz, *The Journal of Physical Chemistry Letters* **2**, 1978–1983 (2011).
- [110] G. Picardi et al., *The European Physical Journal Applied Physics* **40**, 197–201 (2007).
- [111] P. Uebel et al., *Applied Physics Letters* **103**, 021101 (2013).
- [112] M. D. Sonntag et al., *The Journal of Physical Chemistry Letters* **5**, 3125–3130 (2014).
- [113] N. C. Lindquist et al., *Laser & Photonics Reviews* **7**, 453–477 (2013).
- [114] T. Mino, Y. Saito, and P. Verma, *ACS nano* **8**, 10187–10195 (2014).
- [115] B. Pettinger et al., *Physical Review B* **76**, 113409 (2007).
- [116] B. Ren, G. Picardi, and B. Pettinger, *Review of Scientific Instruments* **75**, 837–841 (2004).
- [117] N. Hayazawa et al., *Japanese Journal of Applied Physics* **46**, 7995 (2007).
- [118] A. Downes, D. Salter, and A. Elfick, *The Journal of Physical Chemistry B* **110**, 6692–6698 (2006).
- [119] T.-a. Yano et al., *Applied Physics Letters* **91**, 121101 (2007).
- [120] P. Z. El-Khoury and W. P. Hess, *Nano letters* **14**, 4114–4118 (2014).
- [121] C. A. Barrios et al., *The Journal of Physical Chemistry C* **113**, 8158–8161 (2009).